Deuterium enrichment of the interstellar medium

Ankan Das [a,*], Liton Majumdar [a], Sandip K. Chakrabarti [b,a], Dipen Sahu [a]

[a] Indian Centre For Space Physics, 43 Chalantika, Garia Station Road, Kolkata 700084, India
[b] S.N. Bose National Center for Basic Sciences, JD-Block, Salt Lake, Kolkata 700098, India

HIGHLIGHTS

- Despite of low D/H, our model shows several species could be heavily fractionated.
- Radial distribution of DCO^+/HCO^+ and N_2D^+/N_2H^+ are studied.
- Deuterated isotopomers of H_2CO & CH_3OH are mainly producing in ice phase.
- Computed column densities of deuterated species are compared with the observations.
- IR & sub-mm transitions of some deuterated species are calculated and are compared.

Keywords:
Astrochemistry
Spectra
ISM: molecules
ISM: abundances

ABSTRACT

Despite the low elemental abundance of atomic deuterium in the interstellar medium (ISM), observational evidence suggests that several species, both in the gas phase and in ices, could be heavily fractionated. We explore various aspects of deuterium enrichment by constructing a chemical evolution model in both gaseous and granular phases. Depending on various physical parameters, gases and grains are allowed to interact with each other through the exchange of their chemical species. It is known that HCO^+ and N_2H^+ are two abundant gas phase ions in the ISM and, their deuterium fractionation is generally used to predict the degree of ionization in the various regions of a molecular cloud. For a more accurate estimation, we consider the density profile of a collapsing cloud. The radial distributions of important interstellar molecules, along with their deuterated isotopomers, are presented. Quantum chemical simulations are computed to study the effects of isotopic substitution on the spectral properties of these interstellar species. We calculate the vibrational (harmonic) frequencies of the most important deuterated species (neutral and ions). The rotational and distortional constants of these molecules are also computed in order to predict the rotational transitions of these species. We compare vibrational (harmonic) and rotational transitions as computed by us with existing experimental and theoretical results. It is hope that our results will assist observers in detecting several hitherto unobserved deuterated species.

1. Introduction

The study of deuterium enrichment received a major boost after the discovery of singly or multiply deuterated H_2CO and CH_3OH in the Interstellar Medium (ISM). Interestingly, the fractionation ratios of these deuterated species are often a cross elemental D/H ratio of the ISM ($\sim 1.5 \times 10^{-5}$, Linsky et al., 1995). Earlier work by Hasegawa et al. (1992), Chakrabarti et al. (2006a,b), Das et al. (2008a, 2010), Cuppen and Herbst (2007) and Das and Chakrabarti (2011) suggested that grain chemistry plays a crucial role in the chemical composition of the ISM. The role of grain chemistry in deuterium enrichment has been also highlighted by various authors (Caselli, 2002a; Cazaux et al., 2010; Das et al., 2013a). In the gas phase, the basic reactions are followed by dominant ion-molecular reaction pathways. Around the cold, dense region of the cloud, CO and O are heavily depleted from the gas phase. A strong correlation between CO depletion and deuterium fractionation has been observed (Bacmann et al., 2003; Crapsi et al., 2005). Moreover, the ionization of the ISM could be traced by observing some deuterated ions, such as, DCO^+ and N_2D^+ (Caselli, 2002a). Deuterium chemistry is, therefore, extremely important for tracing the dynamic properties of a cloud.

Aikawa et al. (2005) and Das et al. (2008b, 2013b) have already discussed how the chemical composition of a cloud affects its

* Corresponding author.
E-mail addresses: ankan@csp.res.in (A. Das), liton@csp.res.in (L. Majumdar), chakraba@bose.res.in (S.K. Chakrabarti), dipen@csp.res.in (D. Sahu).

dynamic parameters. Over the last two decades, several attempts have been made to differentiate the evolutionary stages of proto-stars. For example, Lada and Wilking (1984) defined three classes of proto-stars (Class I, Class II and Class III) which evolve progressively. Andrè et al. (1993) defined another class of proto-stars, namely Class 0, which is the youngest among protostar classes. When Class 0 proto-stars reach a slightly more evolved stage, the source is considered to be a Class 0/I borderline object. These stages are defined by observing the variation in the spectral energy distribution of protostars. A number of studies have been carried out to attempt to find a connection between chemical species abundance and evolutionary stage (e.g., Smith, 1998; Myers et al., 1998). Several of these studies suggest that the deuterium fraction of some ions like N_2H^+ and HCO^+ could be used to define different evolutionary stages (Crapsi et al., 2005; Jϕrgensen et al., 2004). Recently, Majumdar et al. (2013) performed a quantum chemical calculation to obtain the spectral signatures (infrared and electronic absorption spectra) of the precursors of some bio-molecules, such as adenine, alanine and glycine (Chakrabarti and Chakrabarti, 2000a,b; Majumdar et al., 2012). It was found that the spectral signatures of the gas phase significantly differ from those in the ice phase. Das et al. (2013a) discuss different properties of HCOCN and one of its isotopologues, DCOCN. These type of studies could also be carried out for other deuterated species, which could serve as benchmarks for observation.

In this paper, we have presented a systematic approach to determine the chemical evolution of some of the most important deuterated species, and given a complete spectral catalog for detecting these molecules around cold and dense regions of a molecular cloud. The outline of this paper is as follows. In Section 2 models and computational details are presented, the implications of our results are discussed in Section 3 and lastly in Section 4 the conclusions are outlined.

2. Chemical modeling

2.1. Gas phase chemical model

We prepared a large gas-grain chemical network to iteratively study the chemical processes in a molecular cloud. Our gas phase chemical network consists of 6149 reactions amongst 601 species. We mainly follow the UMIST-2006 database (Woodall et al., 2007) for the construction of our gas phase chemical network. Since, in the present context our motivation is to study the deuterium enrichment of the ISM, we use some of the important reactions from UMIST-2006 database and assumthat these reactions would also be possible for the deuterated isotopomers. Reaction rates are calculated with the method used by Woodall et al. (2007). To avoid long computational times, as well as the complexity of handling a large chemical network, we identify some dominant pathways for deuterium enrichment and focus on them. This selection is based on the earlier studies of Albertsson et al. (2013), Roberts and Millar (2000) and Rodgers and Millar (1996a,b). We assume that gas and grains are coupled through accretion and thermal/cosmic ray evaporation processes. Details of these processes are already presented in Das and Chakrabarti (2011) and Das et al. (2013a,b).

2.2. Ice phase chemical model

2.2.1. Accretion

Gas phase species are depleted by their accretion onto interstellar ice. Following Hasegawa et al. (1992), the accretion rate of a gas phase species is given by:

$$k_{acc}(i) = s_i \sigma \nu(i) n(i)\ s^{-1},$$

where, s_i is the sticking coefficient, $n(i)$ is the gas phase concentration, $\nu(i)$ is the thermal velocity of the ith species and σ is the geometrical dust-grain cross section ($\sigma = 4\pi r^2$ where r is the radius of the grain $\sim$1000 Å). In our simulation, we take $s_i = 1$ for all the neutrals, except H_2 and He. It is not certain whether atomic and molecular ions stick to the grain surfaces (Hasegawa et al., 1992; Watson, 1976), and here we consider $s_i = 0$ for the ions.

2.2.2. Binding energies

The chemical enrichment of the interstellar grain mantle solely depends on the binding energies of surface species (Das and Chakrabarti, 2013). The mobility of lighter species such as H, D, N and O mainly dictates the chemical composition of the interstellar grain mantle. The composition of the grain mantle, which depends on the mobility of H and O atoms, is already discussed in Das et al. (2008a, 2010) and Das and Chakrabarti (2011). We assume that the gas phase species are physisorbed onto dust grains ($\sim$0.1 μm), having a grain number density of $1.33 \times 10^{-12}\, n_H$, where n_H is the concentration of H nuclei in all forms. The binding energies of deuterated species are assumed to be the same as their hydrogenated counterparts, because the binding energies of deuterated species are unknown. Several theoretical and experimental attempts to find out the diffusive behavior of atomic hydrogen have been made. According to a number of past studies, such as Allen and Robinson (1977), Tielens and Allamandola (1987), Hasegawa and Herbst (1993), Hasegawa et al. (1992) and Chakrabarti et al. (2006a,b), the binding energy for diffusion (E_b) of the H atom was found to be $\sim$ 100 K, whereas for desorption (E_d) it was $\sim$350 K. Following Hasegawa and Herbst (1993), for the H_2 molecule the desorption energy was determined to be $\sim$450 K. According to Hasegawa and Herbst (1993), and references therein, the adsorption energy of N_2 is 1210 K. Caselli (2002a), and references therein, however, suggest that the adsorption energy of N_2 could be 787 K. In our simulation, we consider 787 K to be the adsorption energy for N_2. Desorption energies (E_d) for all other species are taken from the study of Hasegawa and Herbst (1993). Following Tielens and Allamandola (1987) and Hasegawa et al. (1992), we assume E_b=0.3E_d for all other species except for the H atom. To show the importance of these binding energies towards the chemical complexity of the interstellar grain mantle, we construct three sets of binding energies. The first set consists of the binding energies mentioned above, and is labeled set 1. Unless otherwise stated, we always use the set 1 energy values. In set 2, we use results derived by Pirronello et al. (1997, 1999), Katz et al. (1999) for the binding energies (E_b and E_d) of H and H_2 with an olivine grain surface. The difference between set 1 and set 2 is that in set 2 we usd different binding energies (both E_b and E_d) for H, H_2, D, HD and D_2. The binding energies of all other species are similar to those of set 1. Similarly, in set 3, the experimental findings of Pirronello et al. (1997, 1999) are used for the binding

Table 1
Various sets of binding energies.

Species	Set 1		Set 2		Set 3	
	E_b	E_d	E_b	E_d	E_b	E_d
H	100	350	287	373	511	657
H_2	135	450	95	315	163	542
D	100	350	287	373	511	657
HD	135	450	95	315	163	542
D_2	135	450	95	315	163	542
O	240	800	240	800	240	800
OH	378	1260	378	1260	378	1260
H_2O	558	1860	558	1860	558	1860
CO	363	1210	363	1210	363	1210
H_2CO	528	1760	528	1760	528	1760
CH_3OH	618	2060	618	2060	618	2060

energies of H and H_2 with an amorphous carbon grain. For clarity, in Table 1 we present these three sets of binding energies. Since for all cases the binding energies of all the species except H, D, H_2, HD, and D_2 are similar, we tabulate the binding energies (E_b and E_d) of these species only. For the sake of completeness we also show the binding energies of some important surface species (O, OH, H_2O, CO, H_2CO, CH_3OH).

2.2.3. Reaction

There are two reaction schemes that are normally considered for surface reactions, the Langmuir–Hinshelwood (LH) mechanism and the Eley–Rideal (ER) mechanism. In the LH scheme, the gas phase species accrete onto a grain and becomes equilibrated with the surface before reacting with another atom or molecule. In the ER reaction scheme, the incident gas phase species collides directly with an adsorbed species on the surface and reacts with that species. In order to react the adsorbed species require sufficient mobility. Surface reaction rate $R_{i,j}$ between surface species i and j occurring due to classical diffusion can be expressed as (Hasegawa et al., 1992),

$$R_{i,j} = k_{i,j}(Rdiff_i + Rdiff_j)n_i n_j n_d,$$

where n_i and n_j are the number of species i and j, respectively, on an average grain, $Rdiff_i$ and $Rdiff_j$ are the diffusion rate (defined as inverse of the diffusion time) and $k_{i,j}$ is the probability for the reaction to happen upon an encounter. The parameter $k_{i,j}$ is, in general, unity for an exothermic reaction without activation energy. For an exothermic reaction with activation energy E_a and at least one light reactant (H,H_2), $k_{i,j}$ can be approximated by the exponential portion of the quantum mechanical probability for tunneling through a rectangular barrier of thickness a,

$$k_{i,j} = exp[(-4\pi a/h)(2\mu E_a)^{1/2}],$$

where μ is the reduced mass and a is taken as 1 Å. For the light reactive species H and H_2, surface migration via tunneling is much faster than that due to classical hopping. The time scale for tunneling is given by,

$$t_{tun} = \nu_0^{-1} exp[(4\pi a/h)(2mE_b)^{1/2}] \text{ sec}.$$

For the grain surface reaction network, we primarily follow Hasegawa et al. (1992), Cuppen and Herbst (2007), Das et al. (2010) and Das and Chakrabarti (2011). For deuterium fractionation reaction on the grain surface, we primarily follow Caselli (2002a) and Cazaux et al. (2010).

2.2.4. Thermal evaporation

In our model, the abundances of the surface species can be decreased by thermal evaporation, cosmic ray induced evaporation and non-thermal desorption processes. The rate of thermal evaporation of the surface species 'i' is calculated through the following relation,

$$k_{evap}(i) = \nu_0 exp(-E_d/kT_g) \text{ sec}^{-1}, \quad (1)$$

where ν_0 is the characteristic vibrational frequency $\left(\nu_0 = \sqrt{2n_s E_d/\pi^2 m}\right)$ and T_g is the temperature of the grain. For all cases, we have considered that the total number of sites (N_S) on a grain is 10^6, with a surface density of sites (n_s) of 2×10^{14} cm^{-2}.

2.2.5. Cosmic ray induced evaporation

Cosmic ray induced evaporation (hereafter CRD) is a very efficient route for the transfer of surface molecules into the gas phase during the late stage of chemical evolution. CRD rates are calculated using the expression developed by Hasegawa and Herbst (1993). Following Leger et al. (1985), they assumed that relativistic Fe nuclei with energies 20 – 70 MeV could deposit 0.4 MeV energy to an average dust particle of radius 0.1 μm. Grains could be cooled down through thermal evaporation and radiation processes. For easy inclusion of cosmic ray induced photo-evaporation into their model, they developed the following relation,

$$k_{crd} \sim f(70, K)k_{evap}(i, 70\ K), \quad (2)$$

where $k_{evap}(i, 70\ K)$ is the thermal evaporation rate of surface species 'i' at temperature 70 K, $f(70\ K)$ is fraction of time spent by grains at around 70 K. Following Leger et al. (1985), this is defined as $f(70\ K) = 3.16 \times 10^{-19}$.

2.2.6. Non thermal desorption

As energy is released during some of the reactions, adsorbed species could desorb just after their formation. Garrod et al. (2007) estimated this desorption rate via exothermic surface reactions by considering Rice–Ramsperger–Kessel (RRK) theory. They parameterized non-thermal desorption by assuming an approximation. They assumed that a fraction 'f' of the product species of qualifying reactions will desorb immediately and the rest remain as a surface bound product. Here, we apply this mechanism to all surface reactions which result in a single product. The fraction 'f' is calculated by,

$$f = \frac{aP}{(1+aP)}, \quad (3)$$

where a is the ratio between surface molecule bond frequency to the frequency at which energy is lost to the grain surface. Garrod et al. (2007) adopted similar a values for all species, varying a from 0.01 to 0.1. A value of $a = 0.1$ was labeled as 'high' by Pilling (2006). Kroes and Andersson (2006) carried out molecular dynamics simulations of the irradiation of ice with UV photons. From their data, Garrod et al. (2007) estimated that ~0.9% of recombinations result in desorption. Using the value of $E_D(H2O) = 5700$ K and $E_{reac} = 5.91 \times 10^4$ K, they obtained $a = 0.012$. Recently, Dulieu et al. (2013) found experimentally that 90% of H_2O formed on surfaces with OH + H are directly released into the gas phase (Dulieu et al. 2013). However, this is yet to be verified for other species. Here we consider an extensive gas-grain chemical network. In order to test the effects of the non-thermal desorption mechanism and to constrain the value of a, we investigate models with various values of a : 0, 0.01, 0.05, 0.1. A conservative value of a ($a = 0.05$) is assumed for all surface reactions.

Table 2
Initial surface species abundances.

Species	Abundance
H_2	$5.00 \times 10^{-01}/n_H$
He	$1.00 \times 10^{-01}/n_H$
N	$2.14 \times 10^{-05}/n_H$
O	$1.76 \times 10^{-04}/n_H$
H_3^+	$1.00 \times 10^{-11}/n_H$
C^+	$7.30 \times 10^{-05}/n_H$
S^+	$8.00 \times 10^{-08}/n_H$
Si^+	$8.00 \times 10^{-09}/n_H$
Fe^+	$3.00 \times 10^{-09}/n_H$
Na^+	$2.00 \times 10^{-09}/n_H$
Mg^+	$7.00 \times 10^{-09}/n_H$
P^+	$3.00 \times 10^{-09}/n_H$
Cl^+	$4.00 \times 10^{-09}/n_H$
e^-	$7.31 \times 10^{-05}/n_H$
HD	$1.60 \times 10^{-05}/n_H$
H	1.00×10^{00} cm^{-3}
D	1.00×10^{-01} cm^{-3}

2.3. Results of chemical modeling

Hydrogen molecules are mainly formed in diffuse regions, evolving into molecular clouds through surface chemistry. In this study, we aim to study the chemical evolution of a molecular cloud into dense cores. For this purpose, we adopt the initial conditions of a molecular cloud, where almost all hydrogen nuclei are in the form of molecular hydrogen, and the temperature of gas and dust are assumed to be ∼10 K. Ionization in these regions is mainly governed by Cosmic rays. We adopt an initial condition by following Leung et al. (1984) (Table 2). They considered two sets of initial conditions, namely (i) when metalicity is high and (ii) when metalicity is low. For set (ii), the levels of S, Si, Na, Mg and Fe are assumed to be lower by two orders of magnitude than set (i). Leung et al. (1984) found that the results of set (i) agree better with observed molecular abundances in cool, dense clouds. Here, we also consider a similar initially low metalicity condition. It is assumed that initially all deuteriums are locked in the form HD (just as we assumed that all H are in the form of hydrogen molecules initially). The initial abundance of HD molecule is assumed to be 1.6×10^{-5} with respect to the total number of hydrogen nuclei. The initial abundance of the atomic form of hydrogen and deuterium are considered to be 1 cm^{-3} and 0.1 cm^{-3}, respectively. Unless otherwise stated, we always use initial abundances given in Table 2.

2.3.1. Neutral deuterated species

Fig. 1ab shows the chemical evolution of some important gas phase neutral deuterated species with respect to total hydrogen ($n = n_H + 2 \times n_{H2}$). Here, we assume that the cloud is at $T = 10$ K, with constant number density ($n = 10^4$ cm^{-3}) and visual extinction $A_v = 10$. The solid lines of Fig. 1(a) and (b) represent the chemical evolution of gas phase species, where we have considered CRD and non-thermal desorption effects. Dotted lines are for the cases where we have not considered CRD and non-thermal desorption effects. As expected, CRD and non-thermal desorption serve as an efficient means to maintain a reasonable gas phase abundance during the later stages of the chemical evolution process. Owing to the depletion of gas phase deuterated species, curves show a decreasing trend after achieving a peak value. Solid lines show that the gas phase species are maintained in a steady state because of the effects of CRD and non-thermal desorption. Fig. 1(a) clearly shows that the HD molecule is the most abundant deuterated gas phase species throughout the evolution process. D_2 is also found to be highly abundant. Initially, all deuteriums were locked in the form of the HD molecule. By virtue of the low binding energies at the grain surface, HD and D_2 maintain high abundances during the late stages of the chemical evolution process. Two isotopomers of H_2O (HDO and D_2O) and HCN (DCN and DNC) are found to be significantly abundant in the gas phase. The chemical evolution of several isotopomers of CH_3OH and H_2CO are shown in Fig. 1(b). Singly deuterated isotopomers of methanol (CH_3OD, CH_2DOH) are found to be reasonably abundant. Along with doubly and triply deuterated isotopomers, tetra deuterated isotopomers are found to be produced in gas phase as well. The abundances of HDCO and D_2CO are also significant when CRD and non-thermal desorption effects are considered. These molecules are most likely formed on dust surfaces the during cold, dense pre-collapse period, and are evaporated to the gas phase (Loinard et al., 2000). From Fig. 1(a) and (b), it is clear that when CRD and non-thermal desorption effects are taken into account, the abundances of gas phase species reach a steady state equilibrium at times beyond 10^6 years. Individual species attain their peak values at times of $\sim 1 \times 10^5$ years. Depending on the physical conditions (density and temperature), the accretion rates of the gas phase species change. As per Caselli (2002a), for a normal dust to gas ratio and assuming typical dust grains with radius of 0.1 μm, the *average* time scale for a gaseous species to be deposited onto a grain is,

$$t_D \sim 10^9 \sqrt{(A_X)}/[Sn(H_2)] \text{ years},$$

where A_X is the molecular weight, S is the sticking coefficient and $n(H_2)$ is the number density of molecular hydrogen. The sticking coefficients of all neutral species are assumed to be unity. Results presented in Fig. 1(a) and (b) are for the number density (n_H) $= 10^4$ cm^{-3} (i.e., for $n_{H_2} = 5 \times 10^3$ cm^{-3}). From the above equation the time scale for depleting species from the gas is $\sim 1 \times 10^5$ years. As depletion is inversely proportional to the density, for high density clouds the depletion time would be much shorter.

In Fig. 1(c), the chemical evolution of the most abundant surface species (H_2O, CO, CO_2, H_2CO, CH_3OH), along with their most

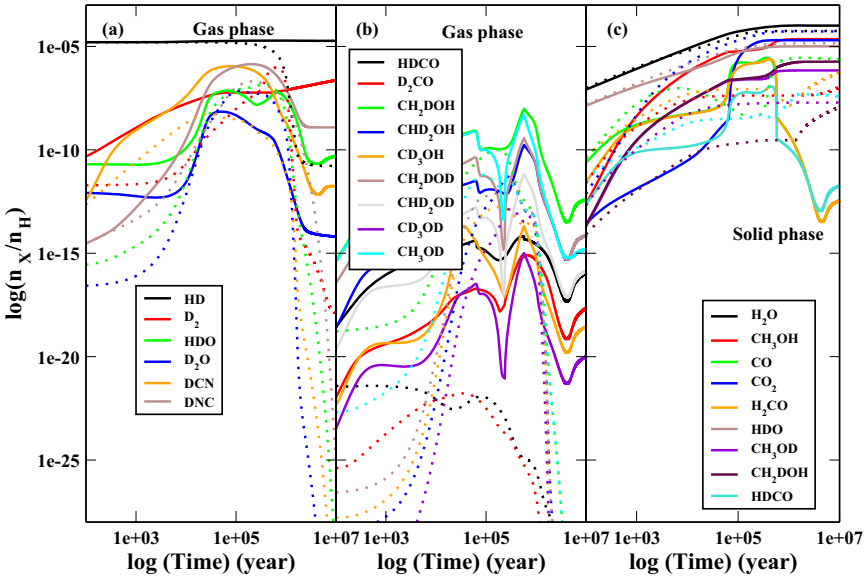

Fig. 1. The chemical evolution of some important gas(a,b) and ice(c) phase neutral deuterated species in the ISM. Solid lines represnent cases where CRD and non-thermal desorption effects are considered and dotted lines are used for cases where these effects are not considered.

abundant deuterated analogues (HDO, HDCO, CH_3OD, CH_2DOH), are shown. As gas phase species are depleted after 2×10^5 years, we obtain a steady state for the abundances of surface species beyond that time. Singly deuterated water, formaldehyde and methanol are found to be heavily abundant. In Fig. 1(b) significant differences in the gas phase abundances of these species for two cases (with and without CRD and non-thermal desorption effects) are distinctly visible. Gas phase abundances of species like methanol and formaldehyde cannot be explained by gas phase chemistry alone. In fact, the sole synthesis path of these species seems to be through production on the surfaces of interstellar grains followed by desorption into the gas. The thermal evaporation process (the binding energies of these species with grain surfaces are higher than ~2000 K, however, is unable to explain the abundances of molecules such as methanol and formaldehyde at around 10 K. It is necessary, therefore to consider non-thermal mechanisms as natural processes. Formaldehyde and methanol are mainly formed by the hydrogenation reaction of CO on interstellar dust grains, and are released in the gas phase in hot core regions. Noble et al. (2012) recently performed experiments to study various desorption processes. Another interesting point to be noted from Fig. 1(c) is that the surface abundances of CH_3OH and its deuterated isotopomers increase when we consider non-thermal desorption processes(solid lines), as in Garrod et al. (2007). It was expected that the inclusion of a non-thermal desorption parameter would increase the gas phase abundances of these species, by virtue of decreasing their surface abundances. Garrod et al. (2007) mentioned that when non-thermal desorption effects were not considered, most of the surface methanol was eventually channeled into CH_4. When non-thermal desorption processes were considered, however, carbon hydrides are allowed to return to the gas phase, where they could convert into CO or its hydrides and maintain a modest level of CO, formaldehyde and methanol in both gas phase and on grain surfaces. In order to study effects of non-thermal desorption on these species, we assumed various '*a*' values and have presented results separately in Fig. 2. Three curves are shown for formaldehyde and methanol, with $a = 0, a = 0.01$ and $a = 0.1$. As expected, for higher '*a*' values, the gas phase abundances of formaldehyde and methanol are enhanced. During the late stages of chemical evolution, the gas phase abundances of these species are significant, due to non-thermal desorption processes. So it is essential to consider non-thermal desorption processes in any gas-grain chemical model, especially in the low temperature regime. From now on, we consider the intermediate value of '*a*', namely $a = 0.05$.

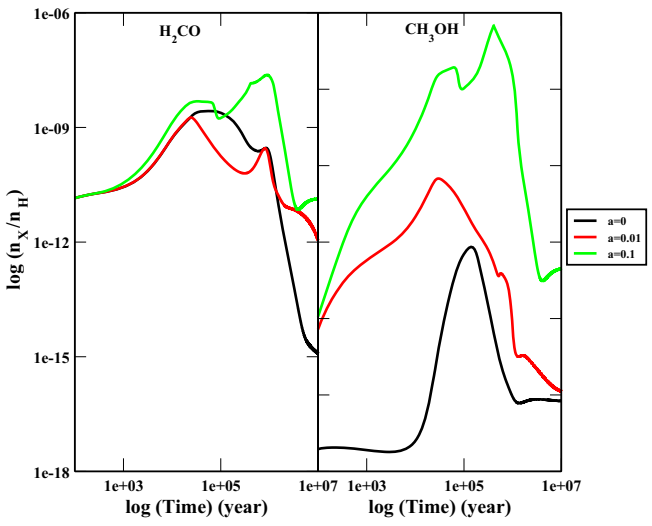

Fig. 2. The chemical evolution of gas phase H_2CO and CH_3OH is shown for various values of '*a*'.

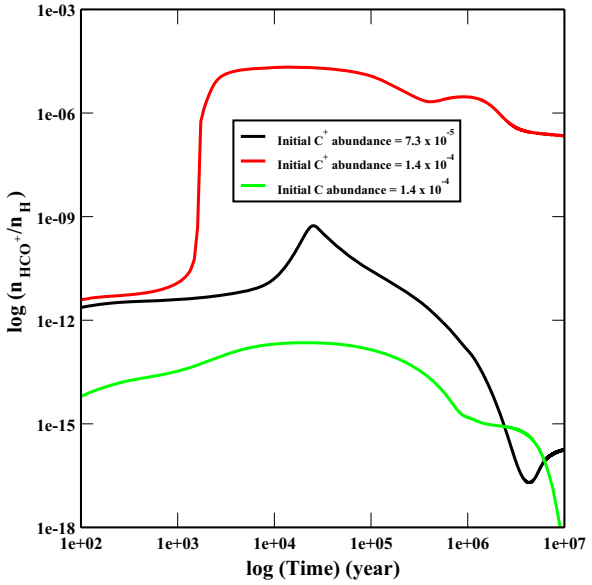

Fig. 3. The chemical evolution of gas phase HCO^+ for various initial carbon abundances.

The chemical composition resulting from our model depends solely on the initial abundances considered. In order to test this feature, we simulate similar physical conditions for a carbon rich environment. Unless otherwise stated, we always consider the initial abundance of C^+ to be 7.3×10^{-5}. To mimic a carbon rich environment, we assume a high carbon abundance initially (1.4×10^{-4} relative to hydrogen nuclei) in ionized (C^+) and in the neutral (C) form. For the purpose of illustration, the chemical evolution of HCO^+ is shown in Fig. 3. Abundances of HCO^+ vary significantly with the choice of initial form (ionized or neutral) and the abundance of carbon. For higher initial C^+ abundance, we have much higher levels of HCO^+, as expected, and for higher neutral carbon abundance, we have much lower levels of HCO^+, also as expected.

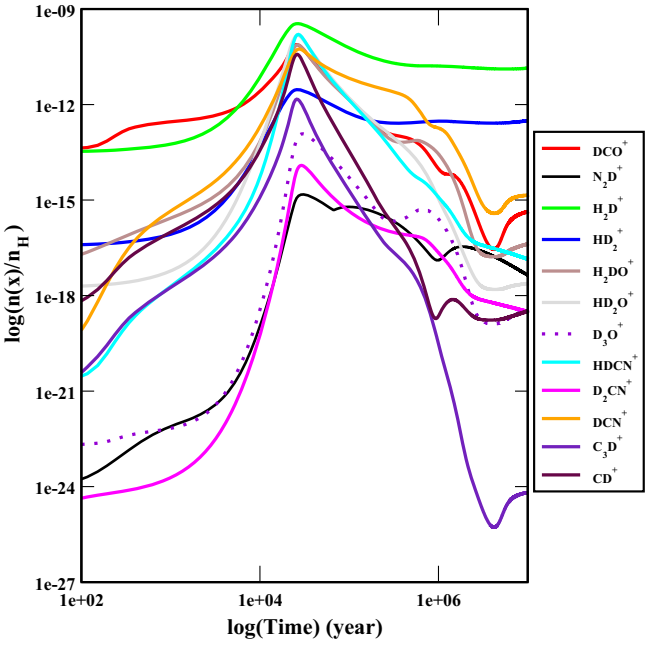

Fig. 4. Important deuterated molecular ions in gas phase.

2.3.2. Deuterated ions

In Fig. 4, we show the chemical evolution of the most important deuterated molecular ions; DCO^+, N_2D^+, H_2D^+, HD_2^+, H_2DO^+, HD_2O^+, D_3O^+, $HDCN^+$, D_2CN^+, DCN^+, C_3D^+ and CD^+. Fig. 4 clearly shows that beyond 2×10^5 years, the abundances of these gas phase deuterated ions decrease gradually. Owing to the depletion of neutrals at around 2×10^5 years, the production of related ions is also heavily hindered. Since recombination rate coefficients (the reaction with electrons) of these ions are much higher ($\sim 10^{-6}$ to 10^{-7} cm^3 s^{-1}), the destruction rate of ions is much faster than the production rate. As a result, ions disappear over the same time scale as the neutrals. Among these ions, DCO^+ and N_2D^+ are widely used to correlate the degree of ionization of the ISM. Fig. 4 shows that the DCO+ molecule is highly abundant in the gas phase. The ratio DCO^+/HCO^+ (hereafter R_1) is widely used as a measure of the limit on electron abundances (x_e) in the ISM. According to Roberts and Millar (2000), at low temperatures DCO^+ is primarily formed via $H_2D^+ + CO \rightarrow DCO^+ + H_2$., but there are other efficient routes for the formation of this species. Here, we have followed pathways mentioned in Albertson et al. (2013) and Roberts and Millar (2000) for the production and destruction of DCO^+. According to Albertsson et al. (2013), major formation routes of DCO^+ are the following,

$$H_2D^+ + CO \rightarrow DCO^+ + H_2,$$
$$HCO^+ + D \rightarrow DCO^+ + H,$$
$$D_3^+ + CO \rightarrow DCO^+ + D_2,$$
$$DOC^+ + H_2 \rightarrow DCO^+ + H_2,$$
$$CH_2D^+ + O \rightarrow DCO^+ + H_2$$

and major destruction routes are the followings,

$$DCO^+ + e^- \rightarrow CO + D,$$
$$DCO^+ + SO \rightarrow DSO^+ + CO,$$
$$DCO^+ + H \rightarrow HCO^+ + D,$$
$$DCO^+ + C \rightarrow CD^+ + CO,$$
$$DCO^+ + HCN \rightarrow HDCN^+ + CO,$$
$$DCO^+ + HNC \rightarrow HDCN^+ + CO.$$

2.3.3. Modeling for a molecular cloud

To obtain results under more realistic conditions, and to obtain the radial distributions of various interstellar species, we now consider that the density profile follows the $\rho \sim r^{-2}$ distribution, as described by Shu (1977). Here we consider that the inner boundary of a protostar is at 100 AU, and the outer boundary was chosen in such a way that density would become 10^4 cm^{-3}. In Fig. 5 the density profile of the collapsing cloud is shown. In our simulations, we evolve the chemical compositions, with various values for the number density of total hydrogen nuclei (n_H), for times up to life time of a generic molecular cloud ($\sim 10^7$ years). For the sake of simplicity, we assume that from the beginning ($t = 0$) this cloud maintains its density profile. Initial conditions are assumed to be similar to the initial conditions of a molecular cloud. We identified up different densities at various regions of the cloud (shown in Fig. 5) and studied the chemical evolution of these regions. For all cases, it was assumed that $T = 10$ K and $A_V = 10$.

In Fig. 6, we show the chemical evolution of CO and N_2 at two different density regions of the cloud. Solid lines are for $n_H = 10^4$ cm^{-3}, and dotted lines are for $n_H = 10^7$ cm^{-3}. For both cases, CO becomes depleted much earlier than N_2. In the case of $n_H = 10^4$ cm^{-3}, at times around $\sim 2 \times 10^6$ years CO molecules are heavily depleted, whereas for $n_H = 10^7$ cm^{-3}, this depletion time scale is shifted by about $\sim 8 \times 10^3$ years. In the case of N_2, depletion features were obtained but higher abundances are maintained during the later stages. This is mainly because of the low binding energy of N_2 ($E_d = 787$ K) with grain surfaces, in comparison to that of CO ($E_d = 1210$ K). Deuterated species can be used to trace slightly warmer region of the core. R_1 is normally used to co-relate the ionization degree (n_e/n_H) of the ISM. Species like CO, however, could be depleted at the dense interior (clearly visible in Fig. 6) and could severely affect R_1. In order to justify the appropriate deuterium fractionation of an entire core, one has to observe molecules that are less affected by depletion, such as N_2H^+ and NH_3. Another benefit of observing N-bearing molecules is that their emission lines are split into hyperfine components, due to the non-zero nuclear spin of nitrogen. This enables the optical depths of the intervening medium to be measured. It is customary to study the ratio N_2D^+/N_2H^+ (hereafter R_2) to get a better approximation around that region.

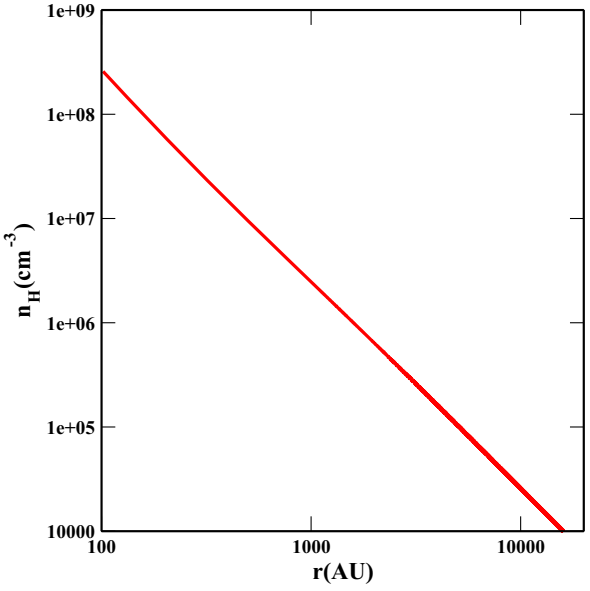

Fig. 5. Density profile of a collapsing cloud.

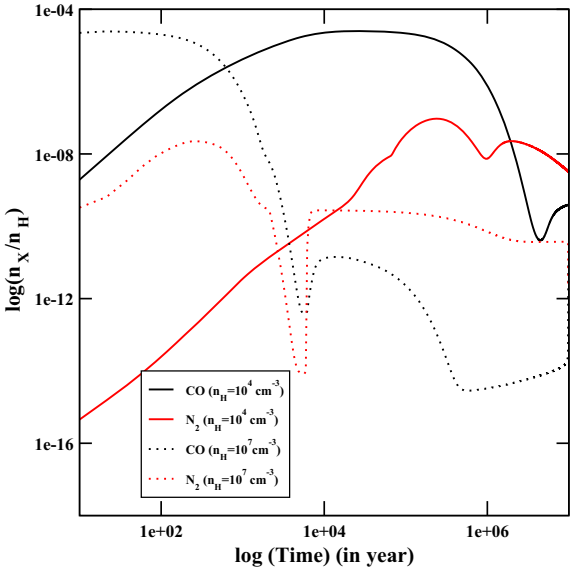

Fig. 6. The chemical evolution of gas phase CO and N_2 for $n_H = 10^4$ cm^{-3} and $n_H = 10^6$ cm^{-3}.

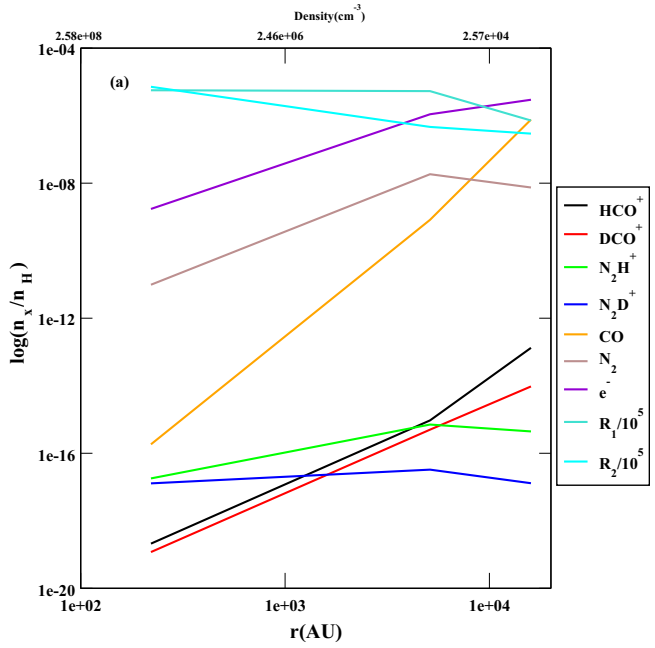

Fig. 7. Radial distributions of some important gas phase ions, R_1, R_2 along with CO, N_2 and e^-.

Fig. 7 shows the abundances of HCO^+, DCO^+, N_2H^+ and N_2D^+ at various depths. These are taken from our simulation results at $t = 10^6$ years. From Fig. 7 it is clear that as the density increases the abundances of all gas phase ions decreases. In Fig. 6, we have shown that N_2 molecules become depleted more slowly, due to lower binding energies. A similar effect is also seen in Fig. 7. Fig. 7 shows that deep inside the cloud CO is heavily depleted. N_2 is also depleted but the rate of depletion is much slower in comparison to CO. As a result CO related species (HCO^+ and DCO^+) become depleted quickly, whereas N_2 related species (N_2D^+ and N_2H^+) deplete very slowly around the dense interior. The radial distributions of R_1 and R_2 along with the abundance of e^- are also shown in Fig. 7. From Fig. 7, it is noted that R_1 remains roughly constant deep inside the cloud, while R_2 steadily increases with depth. This implies that as we go inside the cloud and the density increases, the deuterium fractionation of N_2H^+ becomes favorable. However, in the case of HCO^+, deuterium fractionation roughly remains constant.

In Fig. 8 we plot the electron abundance (a) with respect to R_1 and (b) with respect to R_2. It is has already been mentioned that,

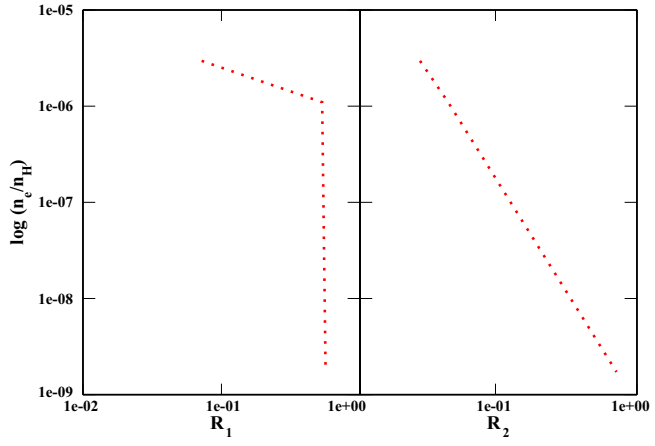

Fig. 8. Electron abundance relative to (a) R_1 and (b) R_2.

due to the heavy depletion of CO and its related species around the dense interior, N_2 related species should be used to predict the degree of ionization (n_e/n_H). We divide the entire zone of the molecular cloud into two parts. The first one is the outer shell (extending from 6000 AU to 20,000 AU) and the second is the dense interior (extending from 100 AU to 6000 AU). R_1 could be used to trace the degree of ionization of the outer shell. From our model, we have electron abundances in the range of $10^{-6} - 3\times 10^{-6}$. From Fig. 8(a), we obtain the following relation between the electron abundance and R_1 between 100 AU to 6000 AU.

$$\frac{n_e}{n_H} = 3.2502 \times 10^{-6} - 4.0302 \times 10^{-6}\ R_1.$$

In the dense interior (100 AU - 6000 AU), R_2 should be used to measure the degree of ionization. From our model, this is in the range of $10^{-9} - 10^{-6}$ in this region. It has the following relation (Fig. 8(b)),

$$\frac{n_e}{n_H} = 6.3773 \times 10^{-6} - 0.00012136\ R_2 + 0.00015693\ R_2^2.$$

In reality, the ionization degree depends on various parameters, and R_1 and R_2 can be used to diagonize it to some extent. Since the abundance of any species depends on various physical conditions and the age of the source, it is very difficult to present any generalized formula for predicting the ionization degree at any particular instant.

So far, a number of theoretical models have tried to correlate the physical properties of protostars with the time since gravitational collapse begins (e.g., Smith, 1998; Myers et al., 1998). The time sequences of evolutionary stages as determined by various models are more or less similar, but absolute ages vary significantly (see Emprechtinger et al. (2008) and references therein). According to Froebrich (2005), the absolute age for Class 0/I borderline objects, for example, varies between 10^4 and 10^5 years. According to Emprechtinger et al. (2008), R_2 is known to trace the evolution of prestellar cores. They proposed that R_2 could be used to trace core evolution even after star formation. According to their work, protostars with $R_2 > 0.5$ are in a stage shortly after they begin to collapse. Later on, R_2 decreases until it reaches a value of 0.03 at the Class 0/I borderline.

Several deuterated molecules are found to be heavily abundant in the ISM. Even water can be highly fractionated. HDO can be formed efficiently on the grain surfaces by the deuteration reaction. Stark et al. (2004) reported the detection of HDO ground transition towards IRAS 16293, and derived a HDO abundance of $\sim 10^{-10}$ in the cold region of the envelope. The measurement of water deuterium fractionation is a relevant tool for understanding the mechanisms of water formation and the evolution from the prestellar phase to the formation of planets and comets (Coutens et al., 2013). Several attempts were made to derive a HDO/H_2O ratio for various Class 0 protostars, which correspond to the main accretion phase, but results turned out to be quite different from one another. Measurements of HDO/H_2O were carried out at two separate zones. For the T> 100 K region of IRAS 16293–2422, Parise et al. (2005) and **?**, Coutens et al. (2013) estimated a HDO/H_2O ratio of a few percent, using single dish observations, whereas Persson et al. (2013) found a much lower estimate (9×10^{-4}), using interferometric data. For the $T < 100$ K region, the ratio of HDO/H_2O was found to be between $3 \times 10^{-3} - 1.5 \times 10^{-2}$ by Coutens et al. (2013).

A large amount of doubly deuterated formaldehyde (D_2CO) has been observed in solar type proto-star IRAS 16293–2422 (Ceccarelli et al., 1998). Turner (1990) found that D_2CO/H_2CO ~0.003 in the Orion compact ridge. It was expected that this high fractionation of D_2CO occurs on the grain surface during the cold phase and that the species evaporate during warm phase. Moreover, a detection of doubly deuterated and triply deuterated

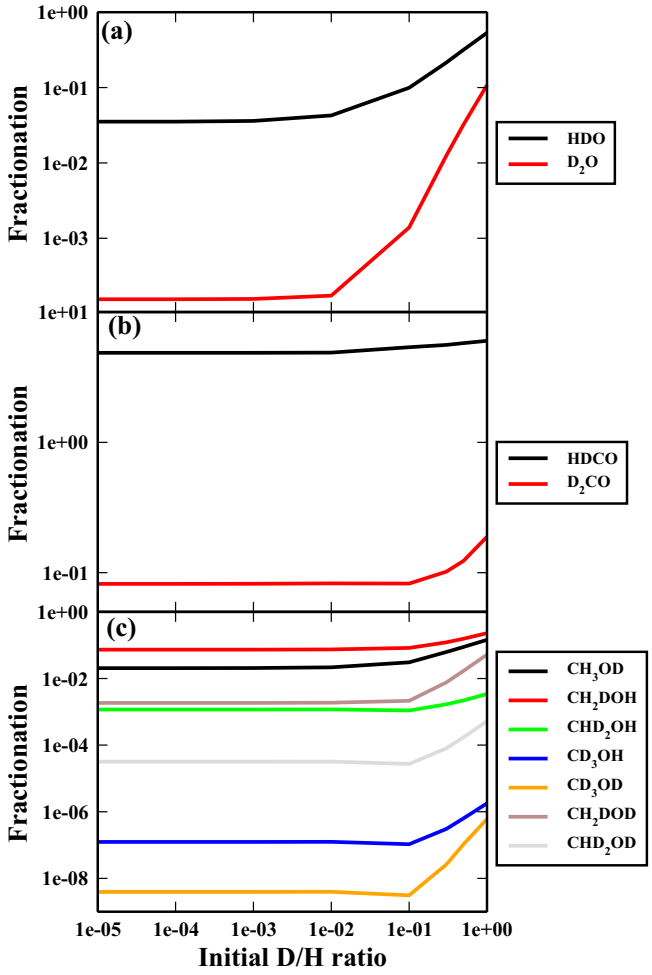

Fig. 9. Deuterium fractionation of the ice phase for the (a) H_2O, (b) H_2CO and (c) CH_3OH molecules.

methanol in low mass protostar IRAS 16293–2422 was reported by Parise et al. (2002, 2004).

In Fig. 9(a)–(c), we show how the deuterium fractionation ratio of some of the major ice phase species changes with variation of the initial atomic D/H ratio the of gas phase. In the study by Roberts et al. (2003) the D/H ratio can reach 0.3. Here, we vary the initial atomic D/H ratio from 10^{-5} to 1 and consider set 1 energy values, $n_H = 10^4$ cm^{-3}, T = 10 K, $A_V = 10$. Deuterium fractionation values are taken at late times (beyond $\sim 10^6$ years). Fig. 9(a)–(c) clearly shows that the singly deuterated parts of H_2O, H_2CO and CH_3OH are heavily fractionated. HDCO fractionation is above unity for most of the simulated time. We notice that at late times (beyond 10^6 years), the abundance of HDCO is enhanced over the abundance of H_2CO. In Caselli et al. (2002b), it was assumed that the activation barriers for the reactions, such as H + CO (E_1) and H + H_2CO (E_2), were in the range of 1000 – 2000 K. For the same reaction with deuterium, i.e. D + CO, the activation barriers differ slightly due to zero point vibrations. They assumed that, for the reaction D + CO, the barrier is $E_1 - 70$ K. For reactions D + H_2CO, H + HDCO, D + HDCO, H + D_2CO and D + D_2CO the energy barriers were considered to be $E_2 - 201$ K, $E_2 - 35$ K, $E_2 - 242$ K, $E_2 - 75$ K and $E_2 - 287$ K, respectively. In this paper, unless otherwise stated, we take $E_1 = E_2 =$ 2000 K. Most recent findings by Fuchs et al. (2009) suggest that the energy barriers (E_1 and E_2) could be much lower than those suggested by Caselli et al. (2002b). According to Fuchs et al. (2009), for the reaction H + CO the activation energy barrier is 390 ± 40 K and for the reaction H + H_2CO it is 415 ± 40 K. In a test case, we have considered $E_1 = 390$ K and $E_2 = 415$ K for the H + CO and H + H_2CO reactions, respectively. Keeping in mind the considerations of Caselli et al. (2002b), the activation energy barriers for D + CO, D + H_2CO, H + HDCO, D + HDCO, H + D_2CO and D + D_2CO reactions become 320 K, 214 K, 380 K, 173 K, 340 K and 128 K, respectively. In reality, the difference in zero point vibrations should depend on the size of the barrier, and for lower barriers these differences should be less. Here, we assume the barrier energies of Caselli et al. (2002b) and the references therein. They assumed that reactions in which D atoms partially replace the H atoms will have different activation energy barriers than E_1 and E_2, due to zero-point vibrations. The zero-point vibration differences were calculated by D. Woon (private communication), and are accurate regardless of the absolute barrier size used for the H + CO and H + H_2CO reactions. According to Kaiser et al. (1999), ab initio calculations show that the isotopic substitution of H by D influences the zero- point vibrational energy. Thus, differences in the activation energy barriers for the above reactions are obvious. Isotopic substitution can modify the rate of reactions in various ways. In many cases, these differences can be rationalized by noting how the mass of an atom affects the vibrational frequency of a chemical bond, even if the electron configuration is nearly identical. Heavier atoms will (classically) lead to lower vibration frequencies, or, viewed quantum mechanically, will have a lower zero-point energy. With a lower zero-point energy, more energy must be supplied to break the bond, resulting in a higher activation energy for bond cleavage, which in turn lowers the measured rate (Carten et al., 2011,2012).

We ran our code for all these sets (set 1, set 2, set 3 and with experimental activation barriers using set 1). To illustrate how

Table 3
Fractionation ratios of the ice phase species for various sets of energies.

Species	Isotopomers	Fractionation ratio (column density in cm^{-2}) by using set 1	Fractionation ratio (column density in cm^{-2}) by using set 2	Fractionation Ratio (column density in cm^{-2}) by using set 3	Fractionation ratio (column density in cm^{-2}) by using experimental activation barrier along with set 1
H_2O	HDO	$9.93 \times 10^{-02} (1.62 \times 10^{17})$	$1.97 \times 10^{-01} (2.47 \times 10^{17})$	$2.11 \times 10^{-02} (4.60 \times 10^{16})$	$6.99 \times 10^{-02} (1.40 \times 10^{17})$
	D_2O	$1.39 \times 10^{-03} (2.26 \times 10^{15})$	$1.10 \times 10^{-04} (1.38 \times 10^{14})$	$9.42 \times 10^{-05} (2.05 \times 10^{14})$	$5.72 \times 10^{-04} (1.15 \times 10^{15})$
H_2CO	HDCO	$5.37 \times 10^{00} (2.89 \times 10^{10})$	$2.08 \times 10^{-01} (1.35 \times 10^{15})$	$5.35 \times 10^{-02} (2.61 \times 10^{16})$	$4.84 \times 10^{02} (9.53 \times 10^{07})$
	D_2CO	$8.24 \times 10^{-02} (4.43 \times 10^{08})$	$7.46 \times 10^{-04} (4.84 \times 10^{12})$	$5.40 \times 10^{-04} (2.63 \times 10^{14})$	$1.10 \times 10^{02} (2.16 \times 10^{05})$
CH_3OH	CH_3OD	$3.06 \times 10^{-02} (1.11 \times 10^{16})$	$4.19 \times 10^{-03} (1.24 \times 10^{15})$	$9.39 \times 10^{-03} (5.22 \times 10^{11})$	$1.01 \times 10^{-02} (6.06 \times 10^{15})$
	CH_2DOH	$8.24 \times 10^{-02} (2.98 \times 10^{16})$	$8.84 \times 10^{-02} (2.62 \times 10^{16})$	$6.12 \times 10^{-02} (3.40 \times 10^{12})$	$1.14 \times 10^{-02} (6.85 \times 10^{15})$
	CHD_2OH	$1.09 \times 10^{-03} (3.94 \times 10^{14})$	$2.55 \times 10^{-04} (7.55 \times 10^{13})$	$7.11 \times 10^{-04} (3.95 \times 10^{10}$	$4.59 \times 10^{-02} (2.75 \times 10^{16})$
	CD_3OH	$1.06 \times 10^{-07} (3.82 \times 10^{10})$	$4.59 \times 10^{-09} (1.36 \times 10^{09})$	$3.97 \times 10^{-07} (2.20 \times 10^{07})$	$2.43 \times 10^{-04} (1.45 \times 10^{14})$
	CD_3OD	$3.11 \times 10^{-09} (1.13 \times 10^{09})$	$2.10 \times 10^{-11} (6.24 \times 10^{06})$	$2.88 \times 10^{-10} (1.60 \times 10^{04})$	$2.98 \times 10^{-06} (1.78 \times 10^{12})$
	CH_2DOD	$2.14 \times 10^{-03} (7.73 \times 10^{14})$	$3.69 \times 10^{-04} (1.10 \times 10^{14})$	$9.52 \times 10^{-02} (1.10 \times 10^{16})$	$2.51 \times 10^{-04} (1.50 \times 10^{14})$
	CHD_2OD	$2.71 \times 10^{-05} (9.80 \times 10^{12})$	$1.16 \times 10^{-06} (3.44 \times 10^{11})$	$6.60 \times 10^{-06} (3.67 \times 10^{08})$	$4.97 \times 10^{-04} (2.98 \times 10^{14})$

the results differ, in Table 3 we present fractionation ratios along with respective column densities for initial atomic D/H ratio 0.1, $n_H = 10^4, T = 10$ K and $A_V = 10$. Furthermore, in Table 3 the variation of these ratios with different energy values is presented. Since for ice phase species we reach a steady state during the late stages of the evolution process, the column densities and fractionation ratios displayed in Table 3 are for late stages of the simulation (after the simulation time is over $\sim 10^7$ years).

3. Quantum chemical model

3.1. Computational details

A significant amount of work is reported in the literature in which the spectroscopic investigation of different interstellar species is guided by theoretical predictions (e.g., Huang and Lee, 2008, 2009; Majumdar et al., 2013, 2014a,b; Das et al., 2013a). Vibrational spectroscopy and rotational spectroscopy are widely used to identify several species of interest. To compute vibrational (harmonic) frequencies, we optimize the geometries of different deuterated neutrals and ions using density functional theory, based on Becke three parameter exchange and the Lee, Yang and Parr correlation functional (B3LYP, Becke, 1993; Lee et al., 1988) with a 6-311++G basis set. We use B3LYP/6–311++G levels of theory for optimization of different interstellar species. Geometry optimization enabled us to locate the minimum energy configuration of these deuterated species. This procedure calculates the wave functions and energy at a starting geometry and then proceeds to search for a new geometry of a lower energy. This is repeated until the lowest energy geometry of these species is found. The procedure calculates forces on each atom of a species by evaluating the gradient of energy with respect to atomic positions. Vibrational frequencies for all these species are also obtained at the same level of the theory, and these frequencies depend on the second derivative of energy with respect to nuclear positions. To study the chemical as well as the spectroscopic properties of all neutral deuterated species in ice phase (water ice), we first optimize geometry of these species at a B3LYP/6–311++G level, with an integral equation formalism variant (IEFPCM) of the default self-consistent reaction field (SCRF) method with a dielectric constant of 78.5. The SCRF calculation using an IEFPCM model, as implemented in the Gaussian 09 W (Frisch et al., 2009) program, was used to include the bulk solvation effect of a medium as water ice. The IEFPCM bulk solvent medium is simulated as a volume of constant dielectric constant (=78.5), which surrounds a solute cavity defined by the union of a series of interlocking spheres centered on the atoms. These methods provide a proper ice phase environment for these neutral deuterated condensed phase species. Here, solute–solvent electrostatic interactions are treated at a dipole level. The solvent effect brings significant changes in the geometrical parameters of these condensed phase deuterated species. Our model confirms that the polarization of the solution has important effects on the absolute and relative solvation energies, which in turn shifts the frequency relative to the gas phase.

To the best of our knowledge, no detailed investigation has been carried out for the computation of different rotational and centrifugal-distortional constants for different deuterated interstellar neutral and ions simultaneously. Usually, these constants are evaluated at the same level as the corresponding force fields needed either for the prediction of vibrational frequencies or vibrational corrections to rotational constants. Here, we use the MP2/6-311++G(d,p) level of theory for performing our calculations. Corrections for interactions between rotational motion and vibrational motion, along with corrections for vibrational averaging and anharmonic corrections to vibrational motion, are also included in our calculations. In brief, we report here the rotational and distortional constants of all important neutral and ionic deuterated species in our model, which are corrected for each vibrational state as well as for vibrationally averaged structures. These rotational constants are required to predict the different rotational transitions, which can be done using the 'SPCAT' program (Pickett, 1991).

3.2. Results of quantum chemical modeling

Several gas phase deuterated molecules have mostly been detected by observing rotational transitions. To simulate these we carried out quantum chemical calculations using the method described in Section 3.1.

A complex pattern of chemical change occurs due to the collapse of a dense cloud core leading to the formation of a young star and its circumstellar disk. Processes such as the depletion of molecules on cold ice grains during the collapsing phase, evaporation of newly-formed species when a protostar starts to heat its surroundings and high temperature reactions in shocked zones created by impacts of outflow all act to cycle molecules from one compound into another. These changes are not only of chemical interest, but can also be used as to diagnose the evolutionary state of an object. Moreover, a knowledge of the chemistry is needed to select appropriate spectroscopic lines in order to trace the physical structure of a particular component. In single-dish observations with 15" – 30" beams, all of these different chemical processes are blurred together, whereas current interferometers with a few arcsec resolution suffer from poor spatial sampling. ALMA, with its unprecedented sensitivity, resolution and UV coverage will be able to image these different chemical regimes and quantitatively address the chemical evolution in the initial stages of star formation. Owing to this, we concentrate only on the 3 to 9 (84 – 720 GHz) band of ALMA. In order to assist in observational identification, in Table 4 we provide different rotational parameters for the most important neutral gas phase deuterated species. These rotational parameters are necessary to predict the spectrum of these species (Pickett, 1991). Among the different neutral deuterated species in Table 4, DNC and DCN are linear molecules. In order to get all the rotational parameters for these species, we need to apply degenerate perturbation theory to correctly compute the bending modes of these species. But as this feature is not implemented in Gaussian 09 W program, we obtain only the single rotational constant (B) for DCN and DNC. Moreover, some rotational transitions which fall in the 84 – 720 GHz (bands 3 – 9 of ALMA) range, are also given in Table 5. The column densities of deuterated species are calculated with the following relation, used by Shalabiea and Greenberg (1994), Das and Chakrabarti (2011) and Das et al. (2013a).

$$N(A) = n_H x_i R,$$

where, n_H is the total hydrogen number density, x_i is the abundance of the ith species and R is the path length along the line of sight ($=1.6 \times 10^{21} A_V)/n_H$). The peak column density of all the neutral deuterated species are presented in Table 5. Observed column densities are also given, with corresponding references. The peak values of ice phase column densities are tabulated along with gas phase column densities. In the case of formaldehyde and methanol, our calculated gas phase column densities differ by some orders of magnitudes from the observed values. Our calculated ice phase column densities may explain this, for example, as per Loinard et al. (2000), the observed column density of HDCO varies between $4.8 \times 10^{13} - 8.1 \times 10^{13}$ cm^{-2}. Our calculated peak value of the gas phase HDCO is 3.23×10^8 cm^{-2}, but the peak value calculated for the ice phase column density is 6.48×10^{15}, which indicates that these types of species are mainly synthesized on dust surfaces at low temperature and could populate gas phase subsequently via

Table 4
Rotational and distortional constants for different neutral deuterated species at the MP2/6-311G++(d,p) level of theory.

Gas phase deuterated species	Rotational constants	Calculated values (in MHz)	Distortional constants	Calculated values (in MHz)
HDO	A	678940.54787	D_J	$0.1086365352 \times 10^{2}$
	B	275198.74337	D_{JK}	$-0.3895959732 \times 10^{2}$
	C	195714.67931	D_K	$0.5654979144 \times 10^{3}$
			d_1	$-0.3994210593 \times 10^{1}$
			d_2	$-0.3131595732 \times 10^{0}$
D_2O	A	445056.83172	D_J	$0.9060508212 \times 10^{1}$
	B	221168.53834	D_{JK}	$-0.4308532587 \times 10^{2}$
	C	147688.78486	D_K	$0.2230651871 \times 10^{3}$
			d_1	$-0.3754958073 \times 10^{1}$
			d_2	$-0.1506205890 \times 10^{0}$
DCN	A	–	D_J	–
	B	35437.934	D_{JK}	–
	C	-	D_K	–
			d_1	–
			d_2	–
DNC	A	–	D_J	–
	B	37466.722	D_{JK}	–
	C	–	D_K	–
			d_1	–
			d_2	–
HDCO	A	199693.34999	D_J	$0.5328503572 \times 10^{-1}$
	B	34528.56786	D_{JK}	$0.1028419257 \times 10^{1}$
	C	29437.69695	D_K	$0.8917367749 \times 10^{1}$
			d_1	$-0.9570179851 \times 10^{-2}$
			d_2	$-0.2627217258 \times 10^{-2}$
D_2CO	A	142634.08807	D_J	$0.4362335359 \times 10^{-1}$
	B	31918.80631	D_{JK}	$0.6360353879 \times 10^{0}$
	C	26081.57265	D_K	$0.414917034 \times 10^{1}$
			d_1	$-0.1031801248 \times 10^{-1}$
			d_2	$-0.2978222074 \times 10^{-2}$
CH_3OD	A	110017.71408	D_J	$0.4614264313 \times 10^{-1}$
	B	23551.47123	D_{JK}	$0.2163668137 \times 10^{0}$
	C	22129.23533	D_K	$0.8855341581 \times 10^{0}$
			d_1	$-0.2682781206 \times 10^{-2}$
			d_2	$0.2173182807 \times 10^{-2}$
CH_2DOH	A	102649.07681	D_J	$0.4204194260 \times 10^{-1}$
	B	22889.94059	D_{JK}	$0.2750167913 \times 10^{0}$
	C	22010.93836	D_K	$0.6689263671 \times 10^{0}$
			d_1	$-0.1443976902 \times 10^{-2}$
			d_2	$0.1103933246 \times 10^{-2}$
CHD_2OH	A	84155.94541	D_J	$0.3517956906 \times 10^{-1}$
	B	21068.30406	D_{JK}	$0.2322462933 \times 10^{0}$
	C	20719.18545	D_K	$0.3896941170 \times 10^{0}$
			d_1	$-0.7434073238 \times 10^{-3}$
			d_2	$0.9511728787 \times 10^{-3}$
CD_3OH	A	70831.43728	D_J	$0.2940531648 \times 10^{-1}$
	B	19919.38820	D_{JK}	$0.1586623951 \times 10^{0}$
	C	19371.86590	D_K	$0.2625638578 \times 10^{0}$
			d_1	$-0.6736522611 \times 10^{-3}$
			d_2	$0.5710887562 \times 10^{-3}$
CH_2DOD	A	90311.79171	D_J	$0.3992772304 \times 10^{-1}$
	B	21697.63492	D_{JK}	$0.1966259292 \times 10^{0}$
	C	22129.23533	D_K	$0.5493414294 \times 10^{0}$
			d_1	$-0.2225437219 \times 10^{-2}$
			d_2	$0.2323808569 \times 10^{-2}$
CHD_2OD	A	75426.27536	D_J	$0.3428624222 \times 10^{-1}$
	B	19810.90663	D_{JK}	$0.1734390959 \times 10^{0}$
	C	19611.52641	D_K	$0.3206028770 \times 10^{0}$
			d_1	$-0.4950184016 \times 10^{-3}$
			d_2	$0.2378618627 \times 10^{-2}$
CD_3OD	A	64997.04836	D_J	$0.2737158018 \times 10^{-1}$
	B	18968.64086	D_{JK}	$0.1232098414 \times 10^{0}$
	C	18049.58590	D_K	$0.2124252221 \times 10^{0}$
			d_1	$-0.1279839822 \times 10^{-2}$
			d_2	$0.1339069324 \times 10^{-2}$

Table 5
Calculated and observed rotational transitions of some neutral gas phase deuterated species.

Neutral deuterated species	Gas phase/ice phase column density (in cm^{-2})	Observed/estimated column density (in cm^{-2})	Tansitions	Calculated frequency (in GHz)	Comparison with (Observation/theory)
HDO	$1.19 \times 10^{15}/1.62 \times 10^{17}$	4.4×10^{13}[e]	1_{01}–0_{00}	470.854	464.924[g]
			2_{02}–1_{01}	941.432	919.3109[g,h]
D_2O	$1.13 \times 10^{14}/2.26 \times 10^{15}$	2.5×10^{12}[j]	1_{01}–0_{00}	368.807	
			2_{02}–1_{01}	737.390	
DCN	$1.78 \times 10^{16}/2.08 \times 10^{16}$	$1.4 \pm 0.3 \times 10^{13}$[e]	2_{02}–1_{01}	141.753	144.8280015[e]
			3_{03}–2_{02}	212.629	217.2385378[e]
			4_{04}–3_{03}	283.505	289.6449170[e]
			5_{05}–4_{04}	354.381	362.0457535[e]
			6_{06}–5_{05}	425.256	
			7_{07}–6_{06}	496.132	
			8_{08}–7_{07}	567.008	
			9_{09}–8_{08}	637.884	
DNC	$2.22 \times 10^{16}/4.89 \times 10^{16}$	1.5×10^{11}[e]	1_{01}–0_{00}	74.933	
			2_{02}–1_{01}	149.867	152.609774[e]
			3_{03}–2_{02}	224.800	
			4_{04}–3_{03}	299.734	
			5_{05}–4_{04}	374.667	
			6_{06}–5_{05}	449.600	
			7_{07}–6_{06}	524.534	
			8_{08}–7_{07}	599.467	
			9_{09}–8_{08}	674.401	
HDCO	$1.07 \times 10^{8}/1.87 \times 10^{15}$	$4.8 - 8.1 \times 10^{13}$[k]	2_{02}–1_{01}	127.93	128.813[a,h]
			3_{03}–2_{02}	191.892	192.893[h]
			4_{04}–3_{03}	255.850	256.586[a,h]
			6_{06}–5_{05}	383.746	382.342[h]
			7_{07}–6_{06}	447.683	444.227[h]
			8_{08}–7_{07}	511.610	505.391[h]
			9_{09}–8_{08}	575.525	565.850[h]
D_2CO	$1.53 \times 10^{7}/2.42 \times 10^{13}$	$1.9 - 5 \times 10^{13}$[k]	2_{02}–1_{01}	115.999	116.68847[f,*j*]
			3_{03}–2_{02}	173.995	174.413[a,h]
			4_{04}–3_{03}	231.988	231.41021[f,h]
			5_{05}–4_{04}	289.977	287.486[a,h]
			6_{06}–5_{05}	347.959	342.52181[f],342.522[j,h]
			7_{07}–6_{06}	405.934	396.517[h]
			8_{08}–7_{07}	463.901	449.596[h]
			9_{09}–8_{08}	521.858	501.983[h]
CH_3OD	$7.70 \times 10^{13}/1.11 \times 10^{16}$	$1.5 \pm 0.7 \times 10^{14}$[c]	2_{02}–1_{01}	91.3	90.703[i]
			3_{03}–2_{02}	137.037	136.026[i]
			4_{04}–3_{03}	182.712	
			5_{05}–4_{04}	228.382	226.539[b,i]
			6_{06}–5_{05}	274.048	
			7_{07}–6_{06}	319.707	
			8_{08}–7_{07}	365.360	
			9_{09}–8_{08}	411.004	
CH_2DOH	$1.51 \times 10^{14}/2.98 \times 10^{16}$	$3.0 \pm 0.6 \times 10^{15}$[c]	2_{02}–1_{01}	89.80	89.4[b]89.25[h]
			3_{03}–2_{02}	134.698	134.112[b],133.847[h]
			4_{04}–3_{03}	179.593	178.342[h]
			5_{05}–4_{04}	224.484	223.422[b],222.741[h]
			6_{06}–5_{05}	269.370	267.634[h]
			7_{07}–6_{06}	314.251	311.211[h]
			8_{08}–7_{07}	359.125	355.292[h]
			9_{09}–8_{08}	403.991	399.295[h]
CHD_2OH	$2.71 \times 10^{12}/3.94 \times 10^{14}$	$6.0 \pm 2.2 \times 10^{14}$[c]	2_{02}–1_{01}	83.573	83.3[b],83.129[i]
			3_{03}–2_{02}	125.358	
			4_{04}–3_{03}	167.141	166.23[i]
			5_{05}–4_{04}	208.920	207.869[b],207.77[i]
			6_{06}–5_{05}	250.696	
			7_{07}–6_{06}	292.466	
			8_{08}–7_{07}	334.231	
			9_{09}–8_{08}	375.990	
CD_3OH	$3.30 \times 10^{8}/3.82 \times 10^{10}$	$7.8 \pm 2.3 \times 10^{13}$[c]	2_{02}–1_{01}	78.581	
			3_{03}–2_{02}	117.870	
			4_{04}–3_{03}	157.157	156.242[d,i]
			5_{05}–4_{04}	196.442	
			6_{06}–5_{05}	235.723	
			7_{07}–6_{06}	275.000	
			8_{08}–7_{07}	314.272	
			9_{09}–8_{08}	353.539	

(*continued on next page*)

Table 5 (*continued*)

Neutral deuterated species	Gas phase/ice phase column density (in cm^{-2})	Observed/estimated column density (in cm^{-2})	Tansitions	Calculated frequency (in GHz)	Comparison with (Observation/theory)
CH_2DOD	$5.71 \times 10^{12}/7.73 \times 10^{14}$		2_{02}–1_{01}	84.512	
			3_{03}–2_{02}	126.766	
			4_{04}–3_{03}	169.018	
			5_{05}–4_{04}	211.266	
			6_{06}-5_{05}	253.510	
			7_{07}–6_{06}	295.749	
			8_{08}–7_{07}	337.982	
			9_{09}–8_{08}	380.208	
CHD_2OD	$1.06 \times 10^{11}/9.80 \times 10^{12}$		2_{02}–1_{01}	78.844	
			3_{03}–2_{02}	118.264	
			4_{04}–3_{03}	157.682	
			5_{05}–4_{04}	197.097	
			6_{06}-5_{05}	236.509	
			7_{07}–6_{06}	275.916	
			8_{08}–7_{07}	315.319	
			9_{09}–8_{08}	354.716	
CD_3OD	$1.57 \times 10^{7}/1.13 \times 10^{09}$		2_{02}–1_{01}	74.035	
			3_{03}–2_{02}	111.052	
			4_{04}–3_{03}	148.066	
			5_{05}–4_{04}	185.078	
			6_{06}–5_{05}	222.088	
			7_{07}–6_{06}	259.093	
			8_{08}–7_{07}	296.095	
			9_{09}–8_{08}	333.092	

[a] Albertsson et al. (2013).
[b] Parise et al. (2002).
[c] Parise et al. (2004).
[d] Parise et al. (2006).
[e] Parise et al. (2009).
[f] Turner (1990) and Ceccarelli et al. (1998).
[g] Neill et al. (2013).
[h] JPL catalog.
[i] NIST catalog.
[j] Coutens et al. (2013).
[k] Loinard et al. (2000).

some energetic event (stellar ejecta, in the hot cores associated with proto-stars, in dense photo-dissociation regions associated with luminous stars, or in the post-shock regions). HDCO, therefore, could be produced during the cold phase of the molecular cloud but when the surrounding cloud become warmer (through some energetic event), ice would sublime and release all the species in the gas phase. We compare our theoretically computed transitions with earlier work and find that some of the transitions match exactly. The calculated column densities of deuterated isotopomers of methanol and H_2CO are found to be very low. These molecules could also efficiently be formed on grain surfaces and could populate the gas phase through some energetic events.

As in the case of gas phase neutral deuterated species, different rotational and distortional constants for deuterated ions are given in Table 6. To obtain all the rotational and distortional constants for linear molecules, such as DCO^+, DCN^+, CD^+ and N_2D^+, it is necessary to use degenerate perturbation theory which could correctly account for bending modes. As mentioned before, this feature is not implemented in GAUSSIAN 09 W program, and we tabulate only the 'B' value for these species. Peak column densities of these gas phase deuterated ions, along with possible rotational transitions in the range of 84 – 720 GHz, are presented in Table 6. A comparison with our computed transitions are highlighted in Table 7.

In order to describe inconsistencies between the transitions reported in this work and other studies (JPL, NIST), we would like to mention that the first step towards the observation of new molecules in the ISM is to obtain transition frequencies. For this, the rotational and distortional constants have to be calculated using a suitable method, and it is always important and advantageous to have a good frequency prediction before an experiment as spectrometers do not generally have automated scanning mode. This significantly reduces the manual scanning time in high resolution spectroscopic observations. Rotational and distortional constants can be calculated using two methods, namely by computational quantum chemistry and experiments. In order to measure experimental rotational spectra of different species at temperatures around 10 K or less (interstellar environment), one can use a cavity Fourier transform, chirped pulse, free jets or stark modulation spectrometers among others. Millimeter wave (30 – 300 GHz) and sub-millimeter wave (300 – 3000 GHz) rotational spectra are most efficiently obtained in the frequency domain with broadband spectrometers. The expected resolution of the rotational spectrum is determined by the Doppler limited line widths of absorption lines, but sometimes also by the experimental techniques used for the detection. Now, most of the rotational and distortional constants reported are obtained by fitting (using the SPFIT program package written by H. M. Pickett of JPL) observed experimental transitions (using the above methods) with a selected Hamiltonian. The SPFIT program provides extended possibilities for the definition of the molecular Hamiltonian required for a particular problem. This program also allows the declaration of spectroscopic parameters for all type of rotors. The fitting program produces an input file with improved spectroscopic constants for the use of the SPCAT program to calculate the spectra. Computational chemistry has greatly enhanced the predictive power for such experiments and observations. For most of the molecular system, exact solution of the Schröinger equation are not possible. Molecular systems that are studied here range from neutral deuterated to ionic deuterated species. The smallest neutral system

Table 6
Rotational and distortional constants for different deuterated ions at the MP2/6–311G++(d,p) level of theory.

Gas phase deuterated species	Rotational constants	Calculated values (in MHz)	Distortional constants	Calculated values (in MHz)
DCO^+	A	–	D_J	–
	B	35483.057	D_{JK}	–
	C	–	D_K	–
			d_1	–
			d_2	–
N_2D^+	A	–	D_J	–
	B	37491.716	D_{JK}	–
	C	–	D_K	–
			d_1	–
			d_2	–
H_2D^+	A	1309800.71258	D_J	0.1699443269×10^3
	B	874168.68952	D_{JK}	0.7270365952×10^3
	C	523857.03868	D_K	0.4076913455×10^3
			d_1	$-0.7957445833 \times 10^2$
			d_2	$-0.2957715880 \times 10^2$
H_2DO^+	A	354117.43200	D_J	0.2947627119×10^1
	B	216974.71900	D_{JK}	0.2864887879×10^2
	C	134526.73411	D_K	$-0.6322042487 \times 10^0$
			d_1	$-0.1844179917 \times 10^1$
			d_2	$-0.9521281691 \times 10^0$
HD_2O^+	A	272194.75777	D_J	0.1776066258×10^1
	B	177205.99078	D_{JK}	0.1791147098×10^2
	C	107323.23142	D_K	0.2835585120×10^1
			d_1	$-0.1169643083 \times 10^1$
			d_2	$-0.6430195000 \times 10^0$
D_3O^+	A	177197.36289	D_J	0.7752981475×10^1
	B	177197.36289	D_{JK}	$-0.13674113745 \times 10^2$
	C	88598.68144	D_K	0.6379112348×10^1
			d_1	$0.2872075808 \times 10^{-8}$
			d_2	$-0.1219005263 \times 10^{-9}$
$HDCN^+$	A	183617.60357	D_J	$0.5652668773 \times 10^{-1}$
	B	38154.03333	D_{JK}	0.4647653905×10^1
	C	31588.56408	D_K	0.8915036310×10^1
			d_1	$-0.2020922328 \times 10^{-1}$
			d_2	$-0.1513073366 \times 10^{-1}$
D_2CN^+	A	131072.14036	D_J	$0.4973302542 \times 10^{-1}$
	B	35460.00741	D_{JK}	0.3119536865×10^1
	C	27908.31506	D_K	0.3792274009×10^1
			d_1	$-0.2531909495 \times 10^{-1}$
			d_2	$-0.1811095002 \times 10^{-1}$
DCN^+	A	–	D_J	–
	B	34105.477	D_{JK}	–
	C	–	D_K	–
			d_1	–
			d_2	–
C_3D^+	A	13126893933.18267	D_J	$-0.4042273088 \times 10_6$
	B	−2415470.80371	D_{JK}	$0.5378663156 \times 10_7$
	C	818347.68409	D_K	$0.2271892620 \times 10^{18}$
			d_1	$0.1691184967 \times 10^{-6}$
			d_2	$-0.2021136560 \times 10_6$
CD^+	A	–	D_J	–
	B	230590.66	D_{JK}	–
	C	–	D_K	–
			d_1	–
			d_2	–

studied in this work is HDO with 3 atoms and 11 electrons. *Ab initio* method MP2 was used in this work, whose computational time scales as N^5 in computational time with the number of electrons N. This method is as accurate as other available methods (Das et al., 2013a; Majumdar et al., 2014a,b). The goal of calculations performed prior to an experiment is to generate coordinates for the nuclei in a molecule. The moment of inertia can be obtained from the coordinates of atoms and their masses. First, the coordinates of the centers of mass are determined, and the principle axes of the system can be determined by diagonalizing the moment of inertia matrix. Once the moment of inertia is determined for the principle axes, the rotational constants can be determined. Symmetric and asymmetric top spectra are known combinations of the rotational constants. The SPCAT program then can be used to generate the spectrum and transitions from rotational and distortional constants. These predictions will be the starting point for all the molecules reported in this work.

Majumdar et al. (2014a) reported the rotational and distortional constants for CH_2CN^-, $CHDCN^-$ and CD_2CN^- in a symmetrically reduced Hamiltonian. Experimental values of these constants were obtained for CH_2CN^- and CD_2CN^- by fitting observed experimental transitions with a Watson S-reduced Hamiltonian using a least

Table 7
Calculated and observed rotational transitions of some deuterated ions.

Important deuterated ions	Gas phase column density (in cm^{-2})	Observed/estimated column density (in cm^{-2})	Transitions	Calculated frequency (in GHz)	Comparison (Observation/theory)
DCO^+	1.23×10^{12}	$4.7 - 40.8 \times 10^{11}$ [c]	1_{01}–0_{00}	70.966	72.039[c,e,ni]
			2_{02}–1_{01}	141.932	144.077[c,ni]
			3_{03}–2_{02}	212.898	216.112[c,ni]
			4_{04}–3_{03}	283.864	288.143[b,ni]
			5_{05}–4_{04}	354.830	360.169[ni]
			6_{06}–5_{05}	425.796	
			7_{07}–6_{06}	496.762	
			8_{08}–7_{07}	567.728	
			9_{09}–8_{08}	638.695	
N_2D^+	2.40×10^{07}	2.310^{12} [be]	1_{01}–0_{00}	74.983	77.109[a,ni]
			2_{02}–1_{01}	149.969	154.217[a,ni]
			3_{03}–2_{02}	224.952	231.322[a,ni]
			4_{04}–3_{03}	299.935	
			5_{05}–4_{04}	374.919	
			6_{06}–5_{05}	449.902	
			7_{07}–6_{06}	524.885	
			8_{08}–7_{07}	599.869	
			9_{09}–8_{08}	674.852	
H_2D^+	5.58×10^{12}	$2 - 40 \times 10^{12}$ [d]			
H_2DO^+	1.20×10^{12}				
HD_2O^+	2.41×10^{12}				
D_3O^+	1.92×10^{09}				
$HDCN^+$	2.55×10^{12}		1_{01}–0_{00}	69.746	
			2_{02}–1_{01}	139.486	
			3_{03}–2_{02}	209.222	
			4_{04}–3_{03}	278.951	
			5_{05}–4_{04}	348.673	
			6_{06}–5_{05}	418.384	
			7_{07}–6_{06}	488.082	
			8_{08}–7_{07}	557.766	
			9_{09}–8_{08}	627.433	
D_2CN^+	1.96×10^{08}		2_{02}–1_{01}	126.738	
			3_{03}–2_{02}	190.099	
			4_{04}–3_{03}	253.455	
			5_{05}–4_{04}	316.802	
			6_{06}–5_{05}	380.139	
			7_{07}–6_{06}	443.463	
			8_{08}–7_{07}	506.773	
			9_{09}–8_{08}	570.067	
DCN^+	8.93×10^{11}		2_{02}–1_{01}	136.433	
			3_{03}–2_{02}	204.641	
			4_{04}–3_{03}	272.851	
			5_{05}–4_{04}	341.062	
			6_{06}–5_{05}	409.273	
			7_{07}–6_{06}	477.484	
			8_{08}–7_{07}	545.695	
			9_{09}–8_{08}	613.906	
C_3D^+	2.37×10^{10}		4_{04}–3_{03}	79.144	
			5_{05}–4_{04}	98.930	
			6_{06}–5_{05}	118.716	
			7_{07}–6_{06}	138.502	
			8_{08}–7_{07}	158.289	
			9_{09}–8_{08}	178.075	
CD^+	6.02×10^{11}		1_{01}–0_{00}	461.181	
			2_{02}–1_{01}	922.362	

[a] Emprechtinger et al. (2008).
[b] Miettinen et al. (2012).
[c] Butner et al. (1995) and Bergman et al. (2010).
[d] Caselli et al. (2008).
[e] JPL catalog, NIST catalog.

square routine Lykke et al. (1987). Majumdar et al. (2014a) mentioned that errors on computed line frequencies are related to the errors on the calculated rotational and distortional constants. There were some uncertainties from experimentally obtained values as well. In this case, Majumdar et al. (2014a) pointed out that these uncertainties could result in an error in between 0.6 MHz and 12 MHz for a frequency range between 18 GHz and 319 GHz. Higher uncertainty was associated with higher frequencies. Here, we observe a similar situation. Tables 5 and 7 clearly show that our results are in agreement at lower frequencies (<200 GHz). Our predicted frequencies for deuterated formaldehyde and methanol are within the error bar of 2 GHz for transitions below 300 GHz. In the case of D_2CO, our calculated transition for $4_{04} \rightarrow 3_{03}$ is at 231.988 GHz, whereas in the JPL catalog this

Table 8
Vibrational frequencies of different isotopomers in the gas/ice phase at the B3LYP/6–311++G level of theory.

Deuterated species in ice Phase	Isotopomers	Peak positions (in cm^{-1}) (Gas phase)	Absorbance	Peak positions (in cm^{-1}) (H_2O ice)	Absorbance	Experimental peak positions (in gas phase) (in cm^{-1})
H_2O	HDO	1378.16	88.6531	1405.66	122.7328	
		2705.63	7.2636	2702.10	15.7450	
		3735.97	19.1116	3727.40	41.5054	
	D_2O	1154.12	54.8490	1176.99	76.6104	
		2619.48	0.8079	2625.06	0.9352	
		2800.44	19.4060	2785.31	43.7223	
H_2CO	HDCO	1045.23	6.7359	1040.78	11.6072	
		1100.30	5.5420	1108.30	7.3579	
		1439.70	8.2712	1431.17	20.5150	
		1677.21	81.6357	1649.89	136.6138	
		2186.27	64.9183	2213.81	68.0555	
		2975.90	89.0502	3014.48	80.8224	
	D_2CO	972.36	1.8692	978.72	2.2770	
		999.70	7.7724	995.53	13.1905	
		1138.09	1.9191	1131.49	5.5560	
		1650.97	75.4535	1623.04	134.8462	
		2132.09	56.4735	2154.89	68.6649	
		2248.26	82.5199	2281.63	75.1423	
CH_3OH	CD_3OD	161.20	99.5390	220.66	142.0151	
		293.34	110.3155	764.12	45.5776	
		386.80	35.4860	884.65	3.6340	
		500.29	58.7503	924.45	75.5395	
		763.50	2.4498	1037.46	17.1796	773.2[a]
		895.12	1.2200	1097.12	4.6425	895[a]
		1048.29	9.7550	1103.99	5.7715	1031.5[a]
		1174.20	47.4951	1126.51	9.9785	1032.56[a]
		2082.62	69.9112	2158.35	39.6044	2077.8[a]
		2214.55	50.2665	2286.64	41.3044	2218.1[a]
		2576.92	22.3665	2326.38	23.5277	
		2838.59	94.7827	2678.17	18.9233	
	CH_2DOD	164.48	100.7205	231.34	134.7124	
		332.46	132.7390	819.72	43.8757	
		392.77	34.8017	925.19	85.1056	
		515.29	63.2073	989.82	21.8331	
		1045.77	7.7157	1173.40	0.8951	1048.5[b]
		1153.64	8.1762	1342.95	7.8599	1162.5[b]
		1176.82	54.5779	1385.44	3.5271	1162.5[b]
		1428.83	12.8712	1506.41	10.0101	1460.5[b]
		2576.98	22.7108	2236.69	40.6041	
		2837.68	126.7372	2677.74	20.6087	
		2883.82	116.3223	3047.59	63.7930	2884 ± 4[b]
		2984.23	109.4862	3134.09	36.2857	2990 ± 4[b]
	CHD_2OD	162.53	99.7778	225.69	139.9513	
		307.05	116.6308	800.46	41.1593	
		389.58	36.0346	886.01	3.8315	
		508.25	58.9529	932.91	101.7461	
		820.84	2.4061	1098.79	0.1321	814.8[b]
		1095.81	16.1715	1110.48	10.2463	1096.4[b]
		1174.20	46.4322	1353.75	10.4653	
		1270.89	13.1683	1369.50	2.3322	
		2135.97	69.7468	2190.28	39.8542	2133[a]
		2577.06	22.0773	2286.72	41.6627	
		2838.39	101.4147	2677.74	20.7812	
		2951.19	110.0932	3125.89	33.0746	2930[a]
	CHD_2OH	165.64	92.4334	292.47	266.3570	
		372.84	169.9004	886.08	3.2353	
		393.54	70.3956	914.18	0.3106	
		583.35	82.7371	945.61	150.2974	
		829.61	2.7927	1110.45	10.4543	
		1100.93	21.6663	1270.82	24.1712	1096.6[b]
		1270.48	16.4612	1353.75	10.5085	1269[b]
		1408.11	71.7012	1393.25	12.8091	
		2135.99	70.2213	2190.34	40.6166	2133.5[a]
		2614.16	44.8765	2286.72	41.4842	
		2951.01	117.0050	3125.42	35.0867	2944.5[a]
		3850.10	131.9254	3677.98	25.2741	
CH_3OH	CH_2DOH	169.30	92.7351	296.56	259.9902	
		384.91	106.3536	905.41	2.0358	
		404.02	146.5793	951.71	149.3625	
		596.94	93.4742	1058.02	9.8248	
		1046.19	6.7389	1284.07	25.1187	1050 ± 2[b]

(*continued on next page*)

Table 8 (*continued*)

Deuterated species in ice Phase	Isotopomers	Peak positions (in cm^{-1}) (Gas phase)	Absorbance	Peak positions (in cm^{-1}) (H_2O ice)	Absorbance	Experimental peak positions (in gas phase) (in cm^{-1})
		1162.78	21.4716	1368.15	8.5425	
		1401.57	68.1558	1390.61	10.2958	
		1435.51	17.0692	1506.54	10.0133	1460 ± 1[b]
		2613.89	48.0499	2236.72	40.9083	
		2883.09	145.3978	3047.58	63.8841	2886 ± 1[b]
		2984.23	110.7735	3133.63	37.9938	2980 ± 5[b]
		3850.11	131.7588	3678.00	25.3322	
	CH_3OD	199.80	213.36	239.23	126.49	
		338.75	100.46	851.97	70.54	
		412.80	18.84	955.71	78.61	
		567.48	99.9472	1153.40	0.4680	
		1046.35	5.8887	1231.89	0.2061	1042.8[a]
		1155.43	15.0893	1485.36	2.5672	1142 ± 3[b]
		1410.22	26.2351	1514.64	11.1257	
		1437.98	53.5992	1522.56	12.4155	1421.3[b]
		2787.74	54.5346	2677.74	20.3561	
		2882.55	149.1114	3013.36	61.4815	2896.5[b]
		2984.23	109.6645	3082.00	68.9276	2970 ± 4[b]
		3613.98	131.49	3138.31	36.6364	
HCN	DCN	616.73	28.3201	628.94	28.1769	
		1943.99	6.7499	1939.11	25.4985	
		2714.94	26.1260	2702.60	35.1536	
HNC	DNC	477.88	113.6888	478.34	131.2467	
		1942.58	34.7245	1955.07	29.1366	
		2886.22	181.4461	2855.45	292.3229	

[a] Serrallach et al. (1974) (Ar matrix data).
[b] Serrallach et al. (1974) (vapour).

transition is tabulated at 231.41021 GHz, so the error is 0.578 GHz. In the case of CH_2DOH our calculated transition for $2_{02} \rightarrow 1_{01}$ is at 89.80 GHz whereas in the JPL catalog this transition is identified at 89.25 GHz and for CH_3OD our calculated transition for $2_{02} \rightarrow 1_{01}$ is at 91.3 GHz whereas in the JPL catalog this transition is at 90.703 GHz. In JPL or NIST, no frequencies for the transitions of for CH_2DOD, CHD_2OD, CD_3OD are presented. Since our computed transitions for singly and doubly deuterated methanols are in good agreement over the lower frequency range (<300 GHz), we hope our computed frequncies will be helpful to detect CH_2DOD, CHD_2OD, CD_3OD in the ISM. These frequencies, along with our computed column densities, could be used to predict the source antenna temperature by using the CASSIS interactive spectrum analyzer (Caux et al., 2011). In order to convert the antenna temperature to the source flux density, following relation can be used,

$$S_v = 3520 \times \frac{T_a}{\eta_A D^2},$$

where, η_A is the the aperture efficiency and D is the diameter. By including all the values, one can obtain the source flux density (S_v). This information would be extremely helpful for the observer in the detection of these species in the ISM.

The theoretical prediction of rotational and distortional constants depends on various choices (Bowman et al., 2007; Carter et al., 2009):

i. Choice of ab initio potentials (dependant on the degrees of freedom),
ii. Choice of ab initio dipole moment surface,
iii. Development of essential quantum methods to calculate vibrational wave functions.

First of all, this is very time consuming and each species requires different a quantum chemical treatment. While computational studies may be feasible for smaller molecular species, extensions to larger molecular systems with additional variables (e.g. mass, charge for ions, etc.) remain a computational challenge. Currently, a full spectral treatment for molecules with more than a few atoms is limited by the availability of effective Hamiltonians, which often do not provide results close to observations or experiments (Carter et al., 2011, 2012). Theoretically computed spectral line-lists provide an essential complement to experimentally measured spectra. One obvious way that theory can complement experiment is in filling in the gaps in laboratory-measurements. Theoretical line-lists can, in principle, span the entire spectral range.

In an earlier section it was pointed out that various deuterated molecules could be trapped inside interstellar ice. The existence of deuterated isotopomers in interstellar ice could be traced by observations through IR telescopes. In order to assist observers, we calculate the vibrational frequencies for various deuterated isotopomers. For this computation, we optimize the geometries of molecules by density functional theory based on the B3LYP method with a 6–311++G basis set in the GAUSSIAN 09 W program. In Table 8, the IR features of various ice phase isotopomers of Water, H_2CO and CH_3OH are given. We have also tabulated gas phase IR features of these isotopomers to highlight spectral changes due to isotopic substitution. In Table 9, we provide the IR features of gas phase deuterated ions. For illustrative purposes, in Fig. 10(a) and (b) we show the IR spectra of gas phase DCO^+, HCO^+, N_2D^+ and N_2H^+, respectively. This figure explains that isotopic substitution plays a dominant role in IR spectral features.

4. Conclusions

Despite the low elemental abundance of atomic deuterium in interstellar space, some species are observed to be heavily fractionated by deuterium. Sometimes the fractionation ratio crosses the observed elemental D/H ratio ($\sim 1.5 \times 10^{-5}$). In order to determine the evolutionary history of deuterated species, we make use of a large gas-grain chemical network. We applied a model simulate the cold dark cloud region of an ISM. Moreover, we have performed

Table 9
Vibrational frequencies of different deuterated ions in gas phase at the B3LYP/6–311++G level of theory.

Gas phase deuterated ions deuterated ions	Peak positions (gas phase) (Wavenumber) (in cm^{-1})	Absorbance
DCO^+	683.57	3.3998
	1897.22	132.8371
	2624.76	25.3446
N_2D^+	628.33	87.6580
	2047.85	49.4619
	2730.37	290.2813
H_2D^+	2230.79	66.6525
	2345.31	317.0829
	3015.87	76.1241
HD_2^+	1946.29	158.8752
	2098.01	87.1753
	2733.51	126.7451
H_2DO^+	566.82	856.4178
	1415.30	118.6293
	1695.32	188.8344
	2675.50	145.2111
	3639.63	201.6169
	3742.37	504.7184
HD_2O^+	518.63	685.2860
	1246.29	79.5791
	1557.51	149.7999
	2599.43	59.0382
	2760.07	265.0375
	3694.16	364.9741
$HDCN^+$	313.84	3.8689
	838.27	94.7313
	970.70	131.1481
	1781.07	12.5791
	2139.99	211.2602
	2867.97	378.5943
D_2CN^+	288.00	1.1228
	742.61	51.1535
	802.03	76.3573
	1737.90	0.3969
	2116.60	159.4864
	2157.11	265.8839
D_3O^+	465.38	515.2134
	1241.35	77.8866
	1241.36	77.8855
	2529.44	0.0000
	2759.90	260.9641
	2759.90	260.9620
CD^+	2011.51	0.9199
C_3D^+	248.79	4.8847
	705.87	2.3408
	711.54	3.0668
	1158.20	54.3460
	2022.23	834.8943
	2605.23	46.2760
DCN^+	617.26	28.3187
	1943.59	6.7620
	2714.08	26.1128

quantum chemical simulation to compute several spectral parameters which could encourage observers to further investigate deuterated species in and around an ISM. In brief, the following highlights of the present work are presented:

- The chemical evolution of deuterated molecules in gas and ice phases are discussed. Computed abundances of the gas phase deuterated isotopomers of formaldehyde, and some isotopomers of methanol, are found to be below present observational limits. However, their abundances in ice phase are significantly higher. It is thought that these ice phase molecules could populate the gas phase through some energetic events, making them detectable.

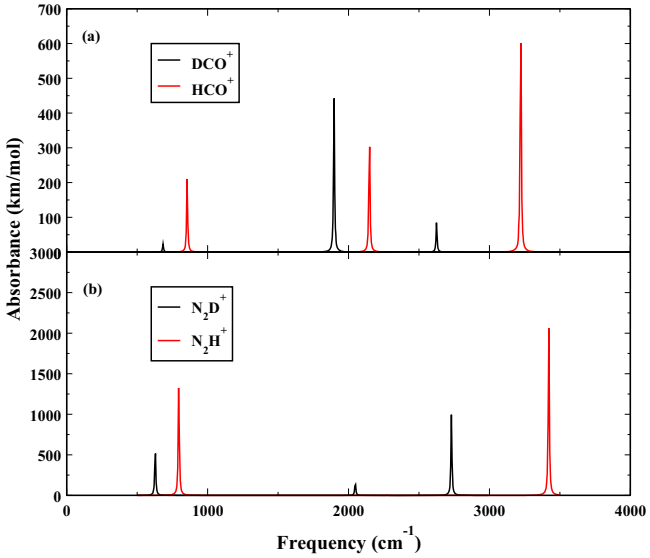

Fig. 10. IR spectra of gas phase (a) HCO^+ and DCO^+ and (b) N_2H^+ and N_2D^+.

- The column densities of deuterated species are computed and compared with observed column densities.
- Rotational and distortional constants for some of the important deuterated species are computed by quantum chemical simulations.
- Rotational and vibrational (harmonic) spectral transitions are calculated for some of the abundant deuterated species and are compared with other theoretical and experimental databases.
- The dependences of the deuterium fractionation of ice phase species for different binding energies and activation energy barriers are discussed.
- Various regions of a collapsing cloud are modeled and the radial distributions of R_1 (DCO^+/HCO^+) and R_2 (N_2D^+/N_2H^+) are studied.

Acknowledgments

AD and DS are grateful to ISRO for financial support through a respond project (Grant No. ISRO/RES/2/372/11–12), SKC acknowledges a DST project (Grant No.SR/S2/HEP-40/2008) for partial financial support and LM thanks the MOES project for his partial financial support. The authors would like to thank an anonymous referee whose valuable suggestions helped to improve this paper significantly.

References

Aikawa, Y., Herbst, E., Roberts, H., Caselli, P., 2005. ApJ 620, 330.
Albertsson, T., Semenov, D.A., Vasyunin, A.I., Henning, T., Herbst, E., 2013. ApJS 207, 27.
Allen, M., Robinson, G.W., 1977. ApJ 212, 396.
Andrė, P., Ward-Thompson, D., Barsony, M., 1993. ApJ 406, 122.
Bacmann, A., Lefloch, B., Ceccarelli, C., Steinacker, J., Castets, A., Loinard, L., 2003. ApJ 585.
Becke, A.D., 1993. J. Chem. Phys. 98, 5648.
Bowman, J.M., Huang, X., Handy, N.C., Carter, S., 2007. J. Phys. Chem. A 111, 7317.
Butner, H.M., Lada, E.A., Loren, R.B., 1995. ApJ 448, 207.
Carter, S., Handy, N.C., Bowman, J.M., 2009. Mol. Phys. 107, 727.
Carter, S., Sharma, A.R., Bowman, J.M., 2011. J. Chem. Phys. 135, 014308.
Carter, S., Sharma, A.R., Bowman, J.M., 2012. J. Chem. Phys. 137, 154301.
Caselli, P., 2002a. P&SS 50, 1133.
Caselli, P., Stantcheva, T., Shalabiea, O., Shematovich, V.I., Herbst, E., 2002b. P&SS 50, 1257.
Caselli, P., Vastel, C., Ceccarelli, C., Van der Tak, F.F.S., Crapsi, A., Bacmann, A., 2008. A&A 492, 703.
Caux, E., Kahane, C., Castets, A., et al., 2011. A&A 532, A23.

Cazaux, S., Cobut, V., Marseille, M., Spaans, M., Caselli, P., 2010. A&A 522, 74.
Ceccarelli, C., Castets, C., Loinard, L., Caux, E., Tielens, A.G.G.M., 1998. A&A 338, L43.
Chakrabarti, S., Chakrabarti, S.K., 2000a. A&A 354, L6.
Chakrabarti, S.K., Chakrabarti, S., 2000b. Ind. J. Phys 74B, 97.
Chakrabarti, S.K., Das, A., Acharyya, K., Chakrabarti, S., 2006a. A&A 457, 167.
Chakrabarti, S.K., Das, A., Acharyya, K., Chakrabarti, S., 2006b. BASI 34, 299.
Coutens, A., Vastel1, C., Cazaux, S., Bottinelli, S., Caux, E., Ceccarelli, Demyk, K., Taquet, V., Wakelam, V., 2013. A&A 553, 75.
Crapsi, A., Caselli, P., Walmsley, C.M., Myers, P.C., Tafalla, M., Lee, C.W., Bourke, T.L., 2005. ApJ, 619.
Cuppen, H.M., Herbst, E., 2007. APJ 668, 294.
Das, A., Chakrabarti, S.K., 2011. MNRAS 418, 545.
Das, A., Acharyya, K., Chakrabarti, S., Chakrabarti, S.K., 2008a. A&A 486, 209.
Das, A., Chakrabarti, S.K., Acharyya, K., Chakrabarti, S., 2008b. NEWA 13, 457.
Das, A., Acharyya, K., Chakrabarti, S.K., 2010. MNRAS 409, 789.
Das, A., Majumdar, L., Chakrabarti, S.K., Chakrabarti, S., 2013a. MNRAS 433, 3152.
Das, A., Majumdar, L., Chakrabarti, S.K., Chakrabarti, S., 2013b. New Astron. 23, 118.
Dulieu, F., Congiu, E., Noble, J., et al., 2013. Nature 3E, 1338.
Emprechtinger, M., Caselli, P., Volgenau, N.H., Stutzki, J., Wiedner, M.C., 2008. A&A 493, 89.
Frisch, M.J.; Trucks, G.W.; Schlegel, H.B., et al., 2009. Gaussian 09, Revision D.01, D.J. Gaussian, Inc., Wallingford CT.
Froebrich, D., 2005. ApJS 156, 169.
Fuchs, G.W., Cuppen, H.M., Ioppolo, S., Romanzin, C., Bisschop, S.E., Andersson, S., van Dishoeck, E.F., Linnartz, H., 2009. A&A 505, 629.
Garrod, R.T., Wakelam, V., Herbst, E., 2007. A&A 467, 1103.
Hasegawa, T., Herbst, E., 1993. MNRAS 261, 83.
Hasegawa, T., Herbst, E., Leung, C.M., 1992. APJ 82, 167.
Huang, X., Lee, T.J., 2008. JChPh 129, 044312.
Huang, X., Lee, T.J., 2009. JChPh 131, 104301.
Jørgensen, J.K., Schier, F.L., van Dishoeck, E.F., 2004. A&A 416, 603.
Kaiser, R.I., Ochsenfeld, C., Head-Gordon, M., Lee, Y.T., 1999. ApJ 510, 784.
Katz, N., Furmann, I., Biham, O., Pironello, V., Vidali, G., 1999. ApJ 522, 305.
Kroes, G.J., Andersson, S., 2006. In: IAU Symp., vol. 231, p. 427.
Lada, C.J., Wilking, B.A., 1984. ApJ 287, 610.
Lee, C., Yang, W., Parr, R.G., 1988. Phys. Rev. B 58, 785.
Leger, A., Jura, M., Omont, A., 1985. A&A 144, 147.
Leung, C.M., Herbst, E., Huebner, W.F., 1984. ApJ 56, 231.
Linsky, J.L., Diplas, A., Wood, B.E., Brown, A., Ayres, T.R., Savage, B.D., 1995. ApJ 451, 335, B35.
Loinard, L., Castets, A., Ceccarelli, C., Tielens, A.G.G.M., Faure, A., Caux, E., Duvert, G., 2000. A&A 359, 1169.
Lykke, K.R., Neumark, D.M., Andersen, T., Trapa, V.J., Lineberger, W.C., 1987. J. Chem. Phys. 87, 6842.
Majumdar, L., Das, A., Chakrabarti, S.K., Chakrabarti, S., 2012. Res. Astron. Astrophys. 12, 1613.
Majumdar, L., Das, A., Chakrabarti, S.K., Chakrabarti, S., 2013. New Astron 20, 15.
Majumdar, L., Das, A., Chakrabarti, S.K., 2014a. A&A 562, A56.
Majumdar, L., Das, A., Chakrabarti, S.K., 2014b. ApJ 782, 73.
Miettinen, O., Harju, J., Haikala, L.K., Juvela, M., 2012. A&A 538, 137.
Myers, P.C., Adams, F.C., Chen, H., et al., 1998. ApJ 492, 703.
Neill, J.L., Wang, S., Bergin, E.A., Crockett, N.R., Favre, C., Plume, R., Melnick, G.J., 2013. ApJ 770, 142.
Noble, J.A., Theule, P., Mispelaer, F., Duvernay, F., Danger, G., Congiu, E., Dulieu, F., Chiavassa, T., 2012. A&A 543, A5.
Parise, B., Ceccarelli, C., Tielens, A.G.G.M., Herbst, E., Leoch, B., Caux, E., Castets, A., Mukhopadhyay, I., Pagani, L., Loinard, L., 2002. A&A 393, L49.
Parise, B., Castets, A., Herbst, E., Caux, E., Ceccarelli, C., Mukhopadhyay, I., Tielens, A.G.G.M., 2004. A&A 416, 159.
Parise, B., Caux, E., Castets, A., et al., 2005. A&A 431, 547.
Parise, B., Ceccarelli, C., Tielens, A.G.G.M., Castets, A., Caux, E., Leoch, B., Maret, S., 2006. A&A 453, 949.
Parise, B., Leurini, S., Schilke, P., Roueff, E., Thorwirth, S., Lis, D.C., 2009. A&A 508, 737.
Persson, M.V., Jrgensen, J.K., van Dishoeck, E.F., 2013. A&A 549, L3.
Pickett, H.M., 1991. J. Mol. Spectrosc. 148, 371.
Pilling, M.J., 2006. In: Faraday Discussions, Chemical Evolution of the Universe, vol. 133, p. 97.
Pirronello, V., Biham, O., Liu, C., Shena, L., Vidali, G., 1997. ApJ 483L, 131.
Pirronello, V., Liu, C., Riser, J.E., Vidali, G., 1999. A&A 344, 681.
Roberts, H., Millar, T.J., 2000. A&A 361, 388.
Roberts, H., Herbst, E., Millar, T.J., 2003. ApJ 591, L41.
Rodgers, S.D., Millar, T.J., 1996a. MNRAS 280, 1046.
Rodgers, S.D., Millar, T.J., 1996b. A&A 438, 585.
Serrallach, A., Meyer, R., Gunthard, Hs. H., 1974. J. Mol. Spec. 52, 94.
Shalabiea, O.M., Greenberg, J.M., 1994. A&A 290, 266.
Shu, F.H., 1977. ApJ 214, 488.
Smith, M., 1998. Ap&SS 261, 169.
Stark, R., Sandell, G., Beck, S.C., et al., 2004. ApJ 608, 341.
Tielens, A.G.G.M., Allamandola, L.J., 1987. In: Hollenbach, D.J., Thronson, H.A., 1987 (Eds.), Interstellar Process. Kluwer, Dordrecht, p. 397.
Turner, B.E., 1990. 362, p. L29.
Watson, W.D., 1976. Rev. Mod. Phys. 48, 513.
Woodall, J., Agndez, M., Markwick-Kemper, A.J., Millar, T.J., 2007. A&A 466, 1197.